Marine Chemistry 176 (2015) 110–125

Contents lists available at ScienceDirect

Marine Chemistry

journal homepage: www.elsevier.com/locate/marchem

The impact of circulation and dust deposition in controlling the distributions of dissolved Fe and Al in the south Indian subtropical gyre

Maxime M. Grand [a,*], Christopher I. Measures [a], Mariko Hatta [a], Peter L. Morton [b], Pamela Barrett [c], Angela Milne [d], Joseph A. Resing [c], William M. Landing [b]

[a] Department of Oceanography, University of Hawaii, Honolulu, HI, USA
[b] Department of Earth, Ocean and Atmospheric Science, Florida State University, Tallahassee, FL, USA
[c] Joint Institute for the study of the Atmosphere and Ocean, University of Washington, PMEL/NOAA, Seattle, WA, USA
[d] School of Geography, Earth and Environmental Sciences, University of Plymouth, Plymouth, UK

ARTICLE INFO

Article history:
Received 4 June 2015
Received in revised form 1 August 2015
Accepted 3 August 2015
Available online 8 August 2015

Keywords:
Fe iron
Al aluminium
Indian Ocean
CLIVAR

ABSTRACT

The South Indian Subtropical Gyre (SISG) is one of the least studied gyre systems of the world ocean with respect to trace elements. Here we report dissolved (<0.45 μm) Fe and Al measurements collected during two high-resolution US-CLIVAR CO_2 Repeat Hydrography sections, which transected the upper 1000 m of the gyre zonally along ~32°S (I05) and meridionally along ~30°E (I06S). Particulate Fe and Al concentrations in waters influenced by the Agulhas Current are also presented. The distributions of dissolved Fe and Al in the gyre are primarily impacted by mineral dust deposition at the surface and the large-scale circulation patterns of the gyre at depth. Using mean mixed layer dissolved Al concentrations, we estimate that the deposition and partial dissolution of mineral dust emanating from South Africa and Australia vary from 60 to 685 mg (dust) m^{-2} yr^{-1} across the 32°S transect. This translates into a dust source of dissolved Fe ranging from 1.7 to 20 μmol Fe m^{-2} y^{-1}. The zonal patterns of aeolian deposition and those of N*, an indirect geochemical tracer for nitrogen fixation, show remarkable similarities along the I05 transect, suggesting that aeolian delivery of Fe may regulate nitrogen fixation rates in the SISG. In the western SISG (west of 60°E), which receives some of the highest aeolian Fe fluxes of the 32°S section, the Fe:AOU ratio in Indian Central Water was elevated relative to that observed in the Indian Central Water occupying the eastern Indian Ocean. These elevated Fe:AOU ratios may reflect the remineralization of Fe-rich organic material from nitrogen fixing organisms at the western end of the basin. Below the mixed layer, the distribution of dissolved Al appears to trace the principal features of the large-scale circulation of the SISG. Elevated subsurface concentrations of dissolved Al (>4 nM) in the southwest Indian Ocean west of 45–50°E are most likely sustained by leakage of Al-rich waters from the Agulhas Return Current. Along the southeast African margin, the elevated particulate Fe (up to 230 nM) and Al (up to 690 nM) concentrations reflect the resuspension and transport of shelf sediments by the highly energetic Agulhas Current. However, while the particulate inputs at the margin are massive and appear to supply modest amounts of dissolved Fe, the distribution of dissolved Al is decoupled from the particulate phase. This observation suggests that the elevated subsurface dissolved Al concentrations observed near the African shelf are not the result of sediment resuspension processes occurring in situ along I05 but are more likely an advected signal originating from the upper reaches of the Agulhas Current.

1. Introduction

The availability of dissolved iron (Fe) plays a significant role in regulating the biogeochemical cycles of carbon and macronutrients in vast regions of the world ocean. In high nutrient low chlorophyll (HNLC) regions, which cover about 30% of the world ocean, several mesoscale Fe enrichment experiments have convincingly demonstrated that phytoplankton growth is limited by the availability of Fe despite ample macronutrient supply (see De Baar et al. (2005), Boyd et al. (2007) and references therein). In oligotrophic regions depleted in macronutrients, there is increasing evidence that enhanced availability of Fe is likely to exert a positive feedback on the activity of nitrogen fixing organisms (Falkowski, 1997; Berman-Frank et al., 2001; Mills et al., 2004; Moore and Doney, 2007; Dutkiewicz et al., 2012; Shiozaki et al., 2014). For example, on a meridional transect across the Atlantic Ocean, Moore et al. (2009) observed that the abundance of diazotrophs

* Corresponding author at: Ocean and Earth Science, National Oceanography Centre Southampton, University of Southampton Waterfront Campus, European Way, Southampton SO14 3ZH, United Kingdom.
E-mail address: maxime@hawaii.edu (M.M. Grand).

http://dx.doi.org/10.1016/j.marchem.2015.08.002
0304-4203/

and nitrogen fixation rates were both significantly correlated with dissolved Fe and aluminium (Al) concentrations, suggesting a pervasive link between aeolian Fe supply and diazotrophic activity. Thus the availability of Fe has far reaching biogeochemical implications from the high to low latitude upper-ocean. An improved understanding of the distribution, sources and internal cycling of Fe in the oceans is therefore required to quantify the impact of Fe availability on contemporary and glacial–interglacial timescales.

In the last decade, the US-CLIVAR-CO_2 Repeat Hydrography (Grand et al., 2014) and GEOTRACES (Anderson et al., 2014) programs have provided basin-scale data for important trace elements and considerably improved the observational database of dissolved and particulate Fe and Al in the Atlantic (Measures et al., 2008a, 2014; Hatta et al., 2014; Rijkenberg et al., 2014; Barrett et al., 2012, 2015), Arctic (Middag et al., 2009; Klunder et al., 2012) and Southern Oceans (Klunder et al., 2011, 2014; Middag et al., 2012, 2013). By contrast, there remain vast areas of the Indian Ocean where dissolved Fe and Al observations are scarce or completely nonexistent. This lack of observations is particularly evident in the South Indian Subtropical Gyre (SISG), most notably in the western gyre and within the Agulhas Current system. At present, the only dissolved Fe and Al data from the SISG consist of three full-depth vertical profiles collected during the GEOTRACES-JAPAN program from 57 to 72°E (Nishioka et al., 2013; Vu and Sohrin, 2013), a high-resolution CLIVAR section in the upper 1000 m of eastern Indian Ocean along 95°E (Grand et al., 2015a,b), and two-full depth soluble Al profiles (<0.04 μm) at the eastern boundary of the SISG near Australia (Obata et al., 2004).

The SISG is an interesting system where the biogeochemical impacts of aeolian deposition in an oligotrophic environment can be evaluated. Numerical models suggest that South Africa and Australia contribute about 10% of global total dust emissions and that the dust emitted from these regions transits primarily over the western and eastern reaches of the gyre (Tanaka and Chiba, 2006; Mahowald, 2007). Recently, Shiozaki et al. (2014) suggested that Fe supplied by aeolian deposition could control nitrogen fixation rates by heterotrophic bacteria in the Indian Ocean. However, satellite aerosol observations suggest that low aerosol concentrations prevail across the SISG (Chin et al., 2014) and there are few estimates of total dust deposition to evaluate the role of atmospheric deposition in supplying dissolved Fe to surface waters of the SISG, estimate its potential impact on nitrogen fixation rates and ascertain the validity of atmospheric model simulations of total deposition (Witt et al., 2010; Grand et al., 2015a). The simultaneous determination of dissolved Fe and Al on selected US-CLIVAR-CO_2 Repeat Hydrography cruises provides a valuable tool to address these questions. Away from the coast and regions subject to deep winter mixing, the principal source of dissolved Fe and Al to the surface ocean is the deposition and partial dissolution of atmospheric dust (Maring and Duce, 1987; Jickells et al., 2005). However, unlike Fe, dissolved Al has no known biological requirement and its relatively long surface residence time can be used to provide a time-integrated picture of the patterns of aerosol deposition in the remote ocean (Measures and Brown, 1996; Measures and Vink, 2000; Grand et al., 2015a).

The dissolved Al imprint resulting from the partial dissolution of mineral dust in the surface ocean is thought to remain confined to the mixed layer. This notion arises from studies of fractional solubility measurements of aerosol laden filters suspended in surface seawater, which show that the majority of dissolvable Al is released in a matter of hours to days (Maring and Duce, 1987; Measures et al., 2010). Hence, the fraction of Al from dust that does not dissolve rapidly in the mixed layer is lost to the sediments via particle settling. Unlike Fe or other bioactive trace elements, there is little evidence that dissolved Al is actively remineralized or desorbed from inorganic or biogenic particle carriers in the main thermocline (Measures and Edmond, 1990; Measures et al., 2008a, 2014; Measures et al., 2014). Thus in the main thermocline and below the mixed layer, the concentration of dissolved Al reflects the balance between dust inputs in regions of water mass subduction, potential inputs from sediment resuspension processes and scavenging removal and mixing along the advective pathway.

This work is mainly concerned with a high-resolution section of dissolved (<0.45 μm) Al and Fe measurements collected in the upper 1000 m of the south Indian subtropical gyre along ~32°S as part of the US-CLIVAR CO_2 Repeat Hydrography I05 cruise. We also discuss data from an earlier meridional cruise in the western Indian Ocean along 30°E (CLIVAR I06S) as well as particulate Fe and Al data (>0.45 μm) from the Agulhas Current region to support the interpretation of several features observed along the I05 section. Using our dissolved Al data from the upper ocean along 32°S, we quantify the magnitude of total dust deposition across the SISG and compare it with composite atmospheric model simulations. We also evaluate the impact of dust deposition on mixed layer dissolved Fe concentrations and implications for nitrogen fixation processes by comparing the zonal patterns of aeolian Fe deposition with that of N*, an indirect geochemical tracer of nitrogen fixation. We also show that the subsurface distribution of dissolved Al is remarkably consistent with the large-scale circulation patterns of water masses occupying the main thermocline of the SISG.

2. Materials and methods

Seawater samples were collected and analyzed aboard the *R/V Roger Revelle* during the CLIVAR-CO_2 Repeat Hydrography I05 and I06S sections using a trace metal clean rosette fitted with twelve, 12 L GO-FLO bottles and following the hydrocast sampling protocol described in Measures et al. (2008b). The CLIVAR I06S section started on February 5, 2008 at the edge of the South African margin at 33°S and continued southward along ~30°E until the Antarctic shelf edge. However, since the trace metal rosette was lost mid-cruise due to rough seas, we only report data from the South African shelf edge to 47.5°S for I06S (Fig. 1). The CLIVAR I05 section, which is the primary focus of this paper, was occupied approximately a year after the I06S cruise. I05 started at the edge of the South African margin on March 17, 2009, transected the SISG along ~32°S and ended near the west Australian continental shelf on May 12, 2009. On the I05 cruise, a total of 86, 12-depth vertical profiles were collected at approximately 1-degree intervals across the upper 1000 m of the SISG (Fig. 1).

Following recovery of the rosette, subsampling of the GO-FLO bottles was carried out in a HEPA filtered environment inside an air-conditioned (~25 °C) laboratory container (Measures et al., 2008b). There, the samples were filtered through 0.45 μm acid-washed 47 mm polycarbonate track-etched filters (GE-Poretics K04CP04700) into 125 mL polymethylpentene (PMP) bottles. Particulate metal concentrations in total suspended matter collected on the filters were analyzed by energy-dispersive X-Ray fluorescence as described in Barrett et al. (2012) and a subset of this dataset is presented in Section 4.3.1. Analysis of dissolved Fe and Al (hereinafter referred to as dFe and dAl) was performed onboard in groups of 12–60 samples using the Flow Injection Analysis (FIA) methods of Measures et al. (1995) and Resing and Measures (1994), respectively. One hour prior to analysis, the PMP bottles containing the filtered samples were acidified with 125 μL of sub-boiled distilled HCl (6 M) and heated to 60 ± 10 °C in a 900 W microwave oven to accelerate the release of complexed Fe. The calibration of the FIA system and drift correction procedures were performed as described in Grand et al. (2015b). The limits of detection, defined as 3 times the standard deviation of replicate analyses of a surface seawater sample, were 0.02 nM for dFe and 0.20 nM for dAl. The analytical precision was approximately 2.5% for dAl at 2.8 nM and 2.0% for dFe at 0.54 nM.

The shipboard dFe dataset of the I05 cruise was validated and corrected by shore-based inductively coupled plasma mass spectrometry (ICP-MS) determinations on a subset of replicate samples brought back to Florida State University and analyzed for dFe using the method of Milne et al. (2010). The accuracy of the ICP-MS dFe determinations was assessed by analyzing the SAFe and GEOTRACES community reference standards and good agreement with the consensus values

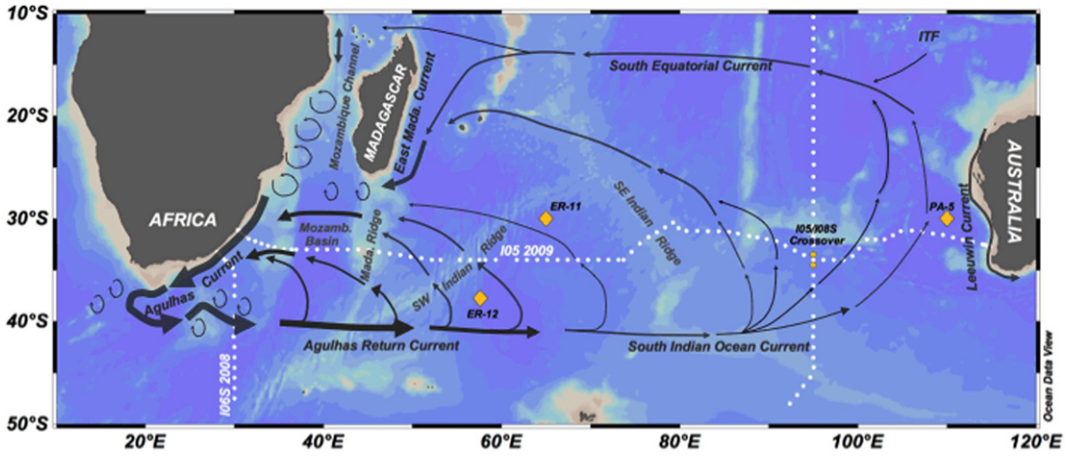

Fig. 1. Large-scale circulation in the upper 1000 m of the SISG after Stramma and Lutjeharms (1997). The dots show the stations sampled during the I05 and I06S (this work) and I08S–I09N cruises (Grand et al., 2015a,b). The diamonds show the stations sampled as part of the GEOTRACES-JAPAN expedition (ER-12 and ER-11) (Vu and Sohrin, 2013; Nishioka et al., 2013) and Piscis Austrinus Expedition (PA-4) (Obata et al., 2004). The I05/I08S crossover points refer to the area where the I05 and I08S (Grand et al., 2015a,b) cruise tracks crossed at 95°E. ITF: Indonesian Throughflow.
Figure prepared using Ocean Data View 4.6.2 (Schlitzer, 2014).

was obtained (Table 1). The shipboard dFe data from each analytical day was corrected using the slope and intercept of a least squares regression between the shore-based ICP-MS and the shipboard dFe values from that day ($n = 12$–24). Fig. 2 shows that the magnitude of the correction subtracted from each sample of the shipboard FIA dataset (i.e., the shipboard FIA system blank) was approximately 70 pM for the I05 cruise. In some cases ($n = 27$), the blank correction applied to the shipboard dataset yielded near surface dFe values that were below the analytical detection limit of the FIA method; these samples were assigned a value equal to the FIA detection limit (0.02 nM). Since we encountered analytical issues with our shipboard FIA system for dFe during the I06S cruise, we report only the shorebased ICP-MS dFe values for that section. We will use the shipboard dAl data from the I06S cruise to discuss the impact of the Agulhas Current system on the dAl concentrations in the westernmost regions of the SISG.

Quality flags were assigned to the dFe and dAl dataset following the WOCE convention, as described in Grand et al. (2015b). In addition, some dFe samples were excluded from the dataset when the comparison with ICP-MS data from replicate stored samples revealed that the sample ran at sea had been contaminated during sampling and/or analysis. When the data from both I05 and I06S are combined, 21% of the dFe samples and 7.5% of the dAl samples were flagged as questionable (WOCE QF = 3) or bad (WOCE QF = 4) and are not included in the interpretation presented here. All the dFe, dAl and ancillary data used in this contribution are publicly available on the CLIVAR & Carbon Hydrographic Data Office website using ExpoCodes 33RR20090320 and 33RR20080204 for I05 and I06S, respectively (www.cchdo.ucsd.edu). The Lowered Acoustic Current Doppler Profiler (LADCP) dataset is available on the SOEST Currents website: http://currents.soest.hawaii.edu/clivar/ladcp/I5S_2009/. The full particulate metals dataset will be published elsewhere and will become available online at a later date.

Table 1
SAFe and GEOTRACES reference standard ICP-MS analyses for dFe. Data are mean ± 1σ and are compared with consensus values as of May 2013.

	This study [nM]	Consensus value [nM]
SAFe S	0.08 ± 0.01	0.09 ± 0.008
SAFe D1	0.59 ± 0.04	0.67 ± 0.04
SAFe D2	0.94 ± 0.03	0.93 ± 0.02
GEOTRACES GS	0.65 ± 0.03	0.55 ± 0.05
GEOTRACES GD	1.03 ± 0.02	1.00 ± 0.10

3. Results

3.1. Hydrographic context

In this section, we describe the large-scale circulation of the SISG and its water mass properties in order to provide the hydrographic context necessary to interpret the distributions of dAl and dFe observed along the I05 and I06S sections (Fig. 1).

3.1.1. South Indian Subtropical Gyre (SISG) circulation

The anticyclonic circulation of the SISG extends from the westward flowing South Equatorial Current near 15°S to the subtropical convergence near 40°S (Fig. 1). The southwestward-flowing Agulhas Current forms the western boundary current of the SISG near the South African shelf edge. The Agulhas starts south of the Mozambique Channel and flows southwestward along the slope of the continental shelf of South Africa. South of the Agulhas Bank, in the Agulhas retroflection region, some Agulhas waters leak into the South Atlantic Ocean in the form of eddies while the remainder is returned to the South Indian

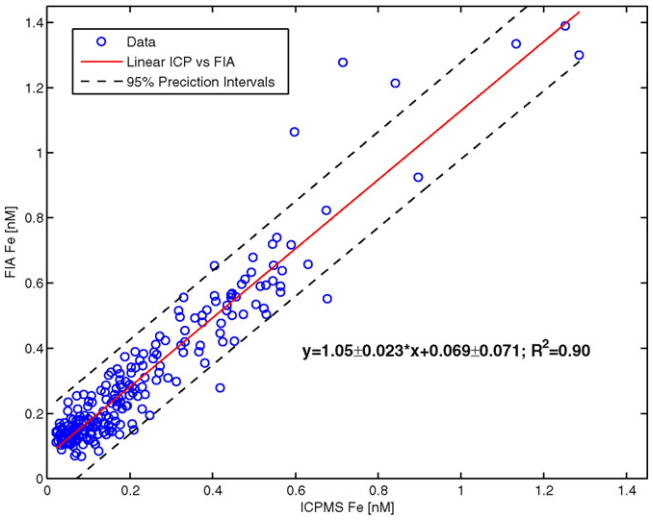

Fig. 2. Shipboard FIA dFe from I05 plotted against ICP-MS dFe measurements. The full line and dashed lines show the least squares fit and 95% prediction intervals, respectively. The slope and intercept of the least squares fit are listed on the plot with their respective standard deviations.

Ocean to form the eastward flowing Agulhas Return Current and ensuing South Indian Ocean Current (Fig. 1).

Unlike its counterparts in the south Atlantic and Pacific Oceans, there is little evidence of an eastern boundary current associated with the south Indian gyral circulation flowing northward along the coast of Australia (Lutjeharms, 2006). Instead, most of the water involved in the gyral circulation recirculates in the western and central parts of the basin while the flow east of 70°E is relatively weak and dispersed. The eastern boundary of the I05 section is impacted by the poleward flowing Leeuwin Current. The Leeuwin Current flows against the prevailing winds along the shelf edge of western Australia (Fig. 1).

In the upper 1000 m, the anticyclonic circulation of the SISG is concentrated in a recirculation cell located in the southwestern part of the basin. This cell is zonally delimited by the African continent and ~70°E and meridionally restricted to the region south of Madagascar and the Agulhas Return Current at its southern edge near 40°S (Fig. 1). We will refer to this recirculation cell as the Southwest Indian Subgyre (Stramma and Lutjeharms, 1997). Most of the water recirculating into the Southwest Indian Subgyre is supplied by leakage from the Agulhas Return Current, which carries waters with identifiable Agulhas characteristics eastward until about 70°E (Lutjeharms and Ansorge, 2001). The majority of the leakage of Agulhas Return Current waters into the Southwest Indian Subgyre (Fig. 1) is thought to occur between 40 and 50°E (Lutjeharms, 2006; Stramma and Lutjeharms, 1997). By the time the Agulhas Return Current reaches 70°E, it is estimated that ~30% of its original volume remains with the balance having been absorbed into the SISG (Lutjeharms and Ansorge, 2001; Lutjeharms, 2006). Beyond 70°E, the remaining flow along the subtropical convergence is named the South Indian Ocean Current (Fig. 1). Another recirculation path is thought to emanate from the South Indian Ocean Current near 90°E (Stramma and Lutjeharms, 1997). There, about half of the transport recirculates northwards towards the Southwest Indian Subgyre while the remaining flow heads northeastwards towards Australia to merge with the South Equatorial Current (Fig. 1). Thus the general circulation of the SISG is characterized by relatively weak and dispersed flow in its eastern reaches and a well-developed recirculation cell west of 70°E, which is fed by leakage from the Agulhas Return Current along its full length (Fig. 1). This circulation has important implications for the water mass characteristics and distribution of dFe and dAl that we observed along the CLIVAR I05 cruise track.

3.1.2. CLIVAR I05: property distributions, boundary currents and water masses

The upper layers of the I05 section exhibit typical subtropical characteristics. The surface layer is filled with Subtropical Surface Water (STSW) of relatively high salinity (>35.5), except near the margins where the advection of Tropical Surface Water (TSW) within the Agulhas and Leeuwin currents results in slightly lower salinities (Fig. 3A). The highest surface salinities were observed east of 73°E and maximum values coincided with northward excursions of the cruise track (Fig. 3A). Nitrate and phosphate concentrations in the mixed layer were generally less than 0.2 μM, except at 2 stations near 97°E where elevated concentrations and anomalously low sea surface temperatures were observed (Fig. 4A). The corresponding drop in sea surface temperatures (Fig. S1), elevated nitrate and phosphate concentrations and shallow mixed layer depths (~20 m, Fig. 4B) near 97°E is consistent with the presence of a cold core eddy entraining nutrient rich deep waters into the mixed layer. A deep chlorophyll maximum was present at the base of the nutricline near 80–100 m at nearly all open ocean stations of the I05 transect (Fig. 3B). The depth of the chlorophyll maximum coincided with a pronounced subsurface oxygen maximum from ~40°E to 100°E, suggesting that this oxygen feature is probably the result of photosynthetic activity (Fig. 3B).

The first five stations of the I05 cruise track near the African shelf (<31.2°E) and the last station at the Australian shelf edge were influenced by the Agulhas and Leeuwin Current systems, respectively. At the western end of the transect, the core of the Agulhas Current extended approximately 50 km offshore from the South African shelf edge. The core manifested itself as a 400 m deep V-shaped region of surface intensified southwestward flow with LADCP velocities exceeding 100 cm s^{-1} in the upper 200 m (data not shown). The southwestward velocities that characterize the Agulhas Current did not extend farther than 145 km offshore, consistent with historical observations of the Agulhas structure in this region (Beal and Bryden, 1999). At the Australian shelf edge, the core of the surface Leeuwin Current was located near 114.5°E and was characterized by LADCP velocities decreasing from 100 cm s^{-1} at the surface to 50 cm s^{-1} at 200 m. Interestingly, the LADCP data did not reveal a clear signature of the Leeuwin Undercurrent, which is usually found below the Leeuwin Current along the upper continental slope (Domingues et al., 2007). The Leeuwin Current usually peaks in intensity in May–June and carries warm (Fig. S1) and low-salinity surface waters from the tropical Indian Ocean and Indonesian Throughflow region poleward along the shelf break of western Australia (Domingues et al., 2007). Although we did not directly sample the core of the Leeuwin Current for trace elements, the highest dFe and dAl levels of the eastern portion of the I05 transect were measured at the edge of the Australian shelf (bottom depth: 210 m), shoreward of the core of the Leeuwin Current (Fig. 3C & D). It is also where we observed the deepest mixed layer depths of the entire cruise track (~100 m, Fig. 4B).

The principal subsurface water masses occupying the thermocline of the I05 section are Subantarctic Mode Water (SAMW), which overlies the characteristic salinity minimum of Antarctic Intermediate Water (AAIW). The density core of AAIW ($\sigma = 27.2$ kg m^{-3}) was only sampled at the first station of the I05 transect and then east of 80°E, where AAIW was shallow enough (<1000 m) for our sampling (Fig. 3A). In the Agulhas Current region, AAIW is saltier and warmer (Fig. S1) than in the eastern reaches of the transect due to the intrusion of high salinity and warm Red Sea Water (Toole and Warren, 1993). The Agulhas Current AAIW also contains higher dFe (~0.6 nM) and lower dAl (~2.5 nM) concentrations than its counterpart at the eastern boundary of the section, where dFe and dAl levels were ~0.5 and 4 nM, respectively (Fig. 3C and D). SAMW is a product of the subantarctic zone of the Southern Ocean formed via deep winter convective mixing. This process generates a thick water mass with relatively uniform temperature/salinity (T/S) properties and high oxygen, which is injected northward into the SISG. Using the criteria of Wong (2005), SAMW (depth > 200 m, potential vorticity < 0.5×10^{-10} m^{-1} s^{-1} and Sigma < 27.00 kg m^{-3}) was identified on the I05 section between ~250 and 570 m east of 57°E (Fig. 3A). West of 57°E, the properties of SAMW have likely been eroded via mixing with recirculating waters in the Southwest Indian Subgyre, consistent with the lower oxygen values observed in this region (Fig. 3B). We did not observe an identifiable thermostad centered at 17 °C west of 40°E previously described as Subtropical Mode Water, unlike the 1987 and 2002 occupations of the I05 section (Toole and Warren, 1993; Fine, 1993; McDonagh et al., 2005) but similar to the 1995 dataset (Donohue and Toole, 2003).

The concentrations of dAl ranged from 1.0 to 18.1 nM in the upper 1000 m of the SISG along 32°S. The highest dAl concentrations were observed at the margins of the basin near the South African (up to 18.1 nM) and Australian shelves (up to 10 nM) (Fig. 3C). Another prominent feature in the dAl distribution is the subsurface region of elevated dAl values (>4 nM) from ~100 to 700 m that extends from the South African margin to the Madagascar ridge near 30–50°E (Fig. 3C). The lowest dAl concentrations (1.0–2.6 nM) were observed in the upper 100 m from 50°E to 74°E, in SAMW near 80°E (<3 nM), and in the density interval occupied by AAIW at the edge of the South African shelf (Fig. 3C). The subsurface minima in dAl observed in the SAMW near 75–80°E may be diagnostic of one of the entry points of SAMW into the SISG (Fig. 3A and C). This type of SAMW, which is ventilated northeast of Kerguelen Island (40°S, 80°E) and is then injected into the SISG west of 80°E (McDonagh et al., 2005; Koch-Larrouy et al., 2010), can be sourced from the northern part of the Antarctic Circumpolar

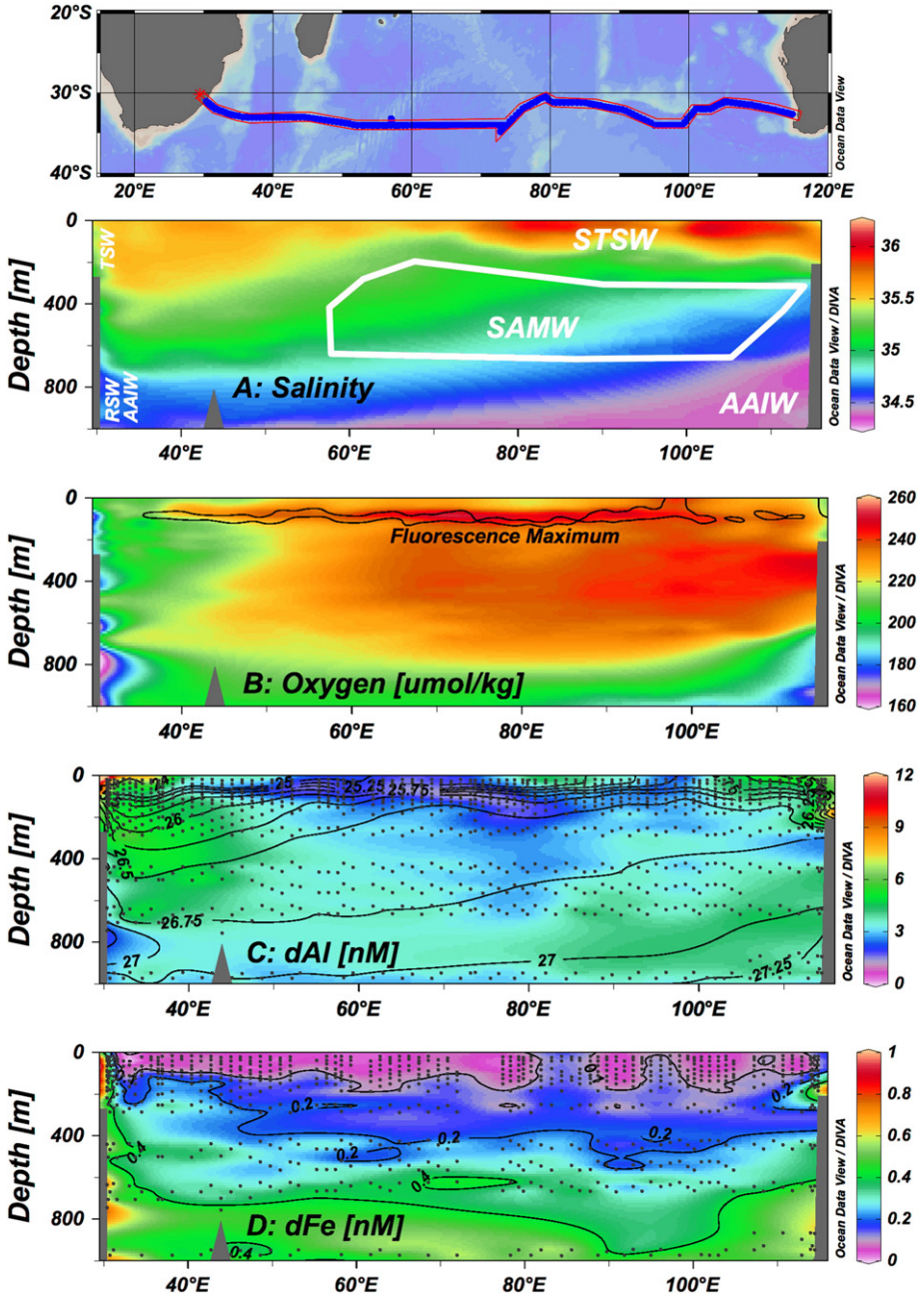

Fig. 3. Upper 1000 m property distributions along I05 (32°S). Black dots show the samples analyzed for dAl and dFe. A: Salinity, the white contour shows the approximate position of SAMW defined using the criteria of Wong (2005). B: Oxygen and subsurface fluorescence maximum shown as black contour, C: dissolved Al overlaid with potential density contours (σ_0 [kg m^{-3}]), D: dissolved Fe shown with selected concentration contours. Acronyms: TSW: Tropical Surface Water; STSW: Subtropical Surface Water; RSW: Red Sea Water; AAIW: Antarctic Intermediate Water; SAMW: Subantarctic Mode Water.
Figure prepared using Ocean Data View 4.6.2. (Schlitzer, 2014).

Current and Agulhas Return Current, where negligible dust inputs result in low dAl surface concentrations (Grand et al., 2015a,b).

The highest dFe concentrations were also observed at the stations nearest to the South African (0.78–1.37 nM) and Australian shelves (0.25–1.04 nM) and decreased offshore. Subsurface dFe levels were relatively elevated west of the Madagascar Ridge (45–50°E), as illustrated by the deepening of the 0.2 nM dFe isopleth east of the ridge (Fig. 3D). The concentrations of dFe in the mixed layer of the SISG were uniformly low from 35 to 80°E (0.05 ± 0.02 nM, $n = 41$) but more patchy east of 80°E with 3 regions centered about 85°E, 95°E and 110°E where mixed layer dFe values were relatively elevated (0.1–0.16 nM, Fig. 3D).

3.1.3. CLIVAR I06S: property distributions and main currents

Only a brief description of the salinity, temperature, and dAl and dFe distributions is presented for the I06S section, since most of our observations are concentrated in the upper 250 m of the water column. On this section, the dFe and dAl concentrations ranged from 0.07 to 1.15 nM and 0.95 to 22 nM, respectively. The highest dFe and dAl concentrations were observed in the northern reaches of the transect and the lowest dAl levels were observed south of 46.5°S (Fig. 5B & C). The first 9 stations of the I06S section near the African shelf edge (north of 34°S) were located within the Agulhas Current. At these stations, relatively warmer and lower salinity Tropical Surface Water

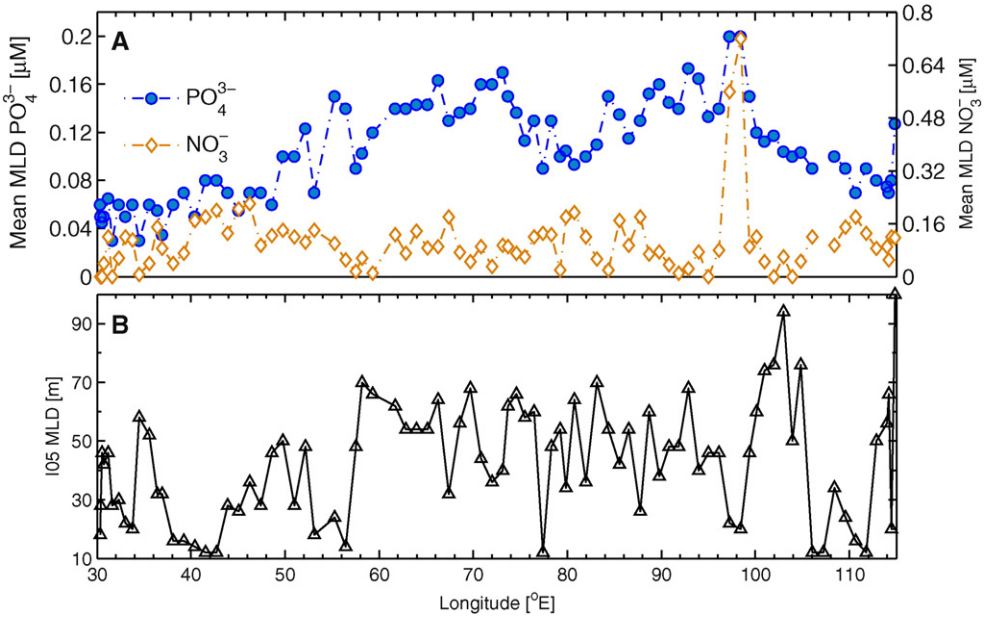

Fig. 4. Mean mixed layer nitrate, phosphate and depth along I05. A: Mean nitrate and phosphate, B: observed mixed layer depth. The depth of the mixed layer was estimated using a density difference of 0.03 kg m^{-3} between 10 m and the base of mixed layer (De Boyer Montégut, 2004). The resulting mixed layer depth was checked and, if necessary adjusted, by inspecting temperature and salinity profiles at each station.

was found in the upper 250 m (Fig. 5A), along with the highest dAl (up to 22 nM) and dFe (up to 1.1 nM) concentrations of the I06S transect. We crossed the Agulhas Front near 40°S. The Agulhas Front coincided with a narrow jet of eastward LADCP velocities extending throughout the upper 850 m at 40°S (Fig. 5D), a 3 °C drop in sea surface temperature and a southward decline in salinity that was most pronounced below 200 m (Fig. 5A). Further south, near 42.5°S, the Subtropical Front (STF) marks the southern limit of the influence of warm, high salinity subtropical waters that are carried eastwards with the Agulhas Return Current (Fig. 5A). In the southwest Indian Ocean, the STF is associated with some of the highest horizontal temperature and salinity gradients of the world ocean (Lutjeharms, 2006), with surface temperature and salinity dropping by 7 °C and 1.51 PSU over 1-degree of latitude as we crossed the STF near 42.5°S during I06S. The position of the STF also coincided with a remarkable gradient in dAl concentrations extending throughout the upper 850 m of the water column (Fig. 5B). Going southward across the STF, surface dAl concentrations decreased by a factor of 3.3.

4. Discussion

In this section, we will first compare our observations with available dFe and dAl data in the South Indian Ocean. We will then focus on the distribution of dAl in the upper layers of the I05 section along 32°S in order to determine the pattern and magnitude of dust deposition to the SISG and implications for dFe cycling and nitrogen fixation processes. We will finally concentrate on the particulate and dissolved Fe and Al distributions in waters influenced by the Agulhas Current and on the elevated subsurface concentrations of dFe and dAl observed in the Southwest Indian Subgyre that appear to terminate near the Madagascar Ridge (Fig. 3C & D).

4.1. Comparison with historical observations

4.1.1. Central south Indian subtropical gyre

There are few trace element data in the SISG against which our observations can be compared (Fig. 1). Near the center of the gyre, Nishioka et al. (2013) and Vu and Sohrin (2013) measured dFe and dAl (<0.2 µm) at 2 stations during the GEOTRACES-JAPAN program (Fig. 1). In general, the dAl data from stations ER-11 and ER-12 were at the lower end of the range of our observations along I05 from the SW Indian Ridge to the SE Indian Ridge (Fig. 6A).

The dFe data from station ER-12 were in excellent agreement with our dFe observations throughout the water column (Fig. 6C). However, the dFe concentrations deeper than the 26.8 kg m^{-3} density surface at station ER-11, which lies ~5° north of the I05 cruise track, were significantly lower than our observations (Fig. 6C), suggesting that there is a decreasing northward gradient in dFe concentrations in the deeper layers (>800 m) of the central south Indian subtropical gyre. The lower deep dFe concentrations in the northern reaches of the SISG may reflect lower remineralization inputs, considering the lower surface productivity inferred from satellite imagery in the northern reaches of the SISG (Fig. 7).

4.1.2. Crossover with the CLIVAR I08S section

The CLIVAR I08S section sampled the eastern reaches of the SISG for dFe and dAl along 95°E two years prior to the I05 occupation (Grand et al., 2015b). Fig. 8 compares our dAl, salinity and dFe observations at 3 stations from I05 and 2 stations from I08S at the crossover point between the cruise tracks (Fig. 1). Although vertical profiles of dAl during I08S and I05 display similar features, the dAl concentrations from I08S were lower than I05 throughout the water column (Fig. 8A). In the SAMW and AAIW density intervals, which are too deep (>400 m) to be influenced by possible inter-annual differences in dust deposition from the overlying surface layer, the dAl data from I08S were on average 1.3 nM lower than on I05. Considering that the I08S and I05 cruise tracks were sampled two years apart, it is possible that the differing subsurface dAl concentrations observed near 95°E reflect temporal variations in the dAl concentrations in SAMW and AAIW. Although an analytical offset between the cruises cannot be entirely ruled out, it is plausible that the SAMW sampled during I05 may have received higher dust inputs in its subduction region compared to the SAMW variety measured during I08S. Except for 5 data points in the upper portion of the water column that coincide with lower salinities during I08S (Fig. 8B & C), the dFe data in SAMW and AAIW at the crossover point of I08S and I05 showed no significant differences (Mann–Whitney U-test). Note that, unlike dAl, the subsurface dFe concentrations in SAMW are unlikely to record potential temporal differences in dust deposition in the

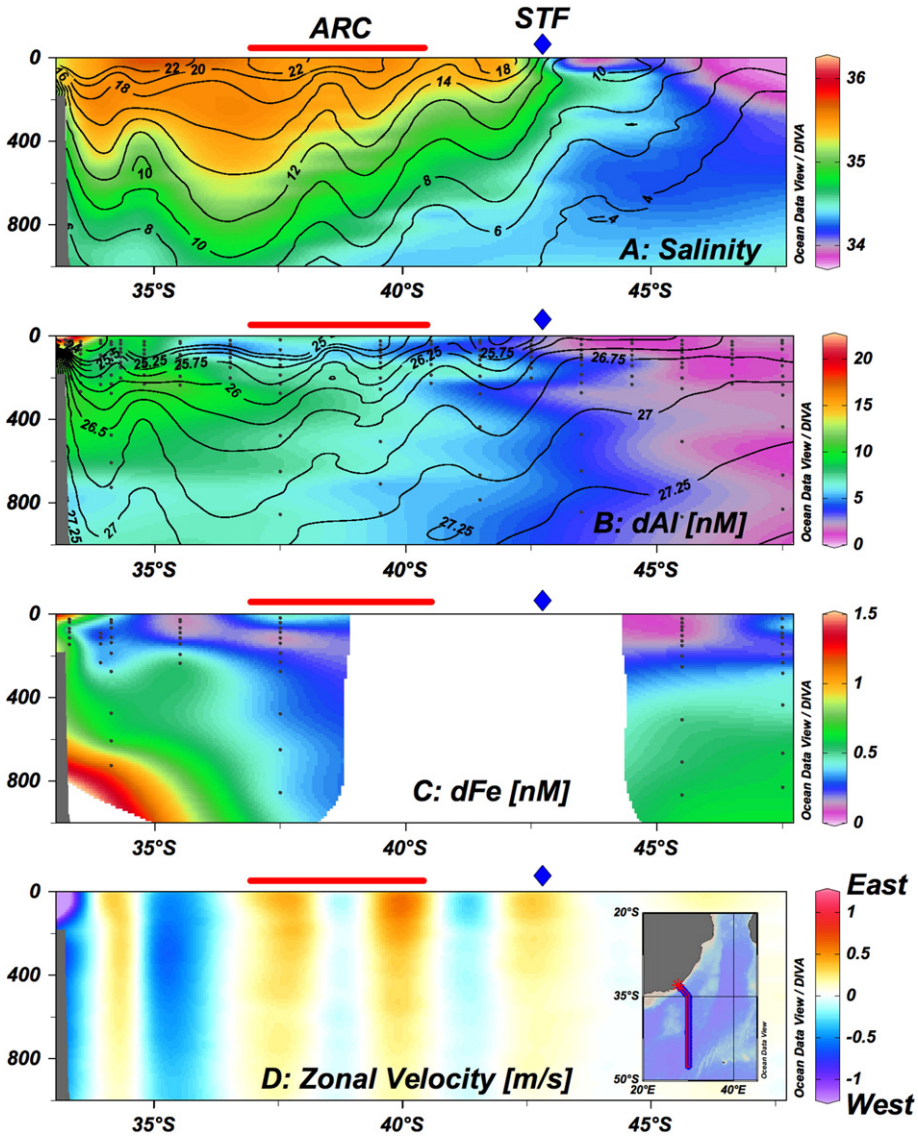

Fig. 5. Upper 1000 m property distributions along I06S (30°E). Black dots show the samples analyzed for dAl and dFe. The diamonds show the position of the Subtropical Front (STF), the red lines show the approximate position of the Agulhas Return Current. A: Salinity overlaid with temperature contours. B: dAl [nM] overlaid with potential density contours (σ_0 [kg m^{-3}]), C: dFe [nM], note that the dFe data were not interpolated from 37 to 45°S due to lack of ICPMS data. D: LADCP zonal velocity [m s^{-1}]. Samples for dFe data were analyzed post-cruise via ICP-MS (see text for details).
Figure prepared using Ocean Data View 4.6.2 (Schlitzer, 2014).

subduction region of SAMW between the I05 and I08S occupations since the residence time of dFe in surface waters is much shorter than that of dAl.

4.1.3. Eastern Indian Ocean

The only other published Al data in the SISG are dissolved Al (<0.04 μm) measurements collected in late 1996 during the Japanese led Piscis Austrinus Expedition (Obata et al., 2004). The vertical dAl profiles of station PA-5 and from 2 neighboring I05 stations showed similar shape characteristics; a surface maximum followed by decreasing dAl concentrations until about ~400 m, with relatively invariant concentrations below that (Fig. 9). From 100 to 400 m, our dAl data were higher than the PA-5 observations and part of the difference may be due to our operational definition of dissolved Al that includes colloidal Al, unlike the data of Obata et al. (2004). However, direct measurements of the colloidal fraction of Al have shown that Al colloids contribute at most to 11% of the dAl pool (Moran and Moore, 1989; Reitmeyer et al., 1996; Dammshäuser and Croot, 2012), suggesting that the higher dAl concentrations (~1 nM) that we observed from 100 to 400 m relative to station PA-5 are unlikely due to the presence of colloidal Al in our samples. Considering the 13 years that separated our sampling from that of Obata et al. (2004), it is more likely that the offset results from temporal variations in the dAl content of subsurface waters.

4.2. Dust deposition along 32°S in the south Indian subtropical gyre

The deposition and partial dissolution of atmospheric dust is the dominant source of dAl to surface waters of the open ocean (Maring and Duce, 1987). Inorganic scavenging removal of dAl onto sinking particulate matter constitutes its principal sink (Moran and Moore, 1992), consistent with the scavenged type profile that many dAl profiles display in the open ocean (Orians and Bruland, 1985; Bruland and Lohan, 2003). Thus the concentration of dAl in the surface waters at a given location of the remote ocean can be used to trace the pattern and estimate the magnitude of total dust deposition because it reflects the steady state balance between the magnitude of dust deposition (i.e., wet + dry) and particulate scavenging removal (Measures and Brown, 1996). In order to calculate total dust deposition across the

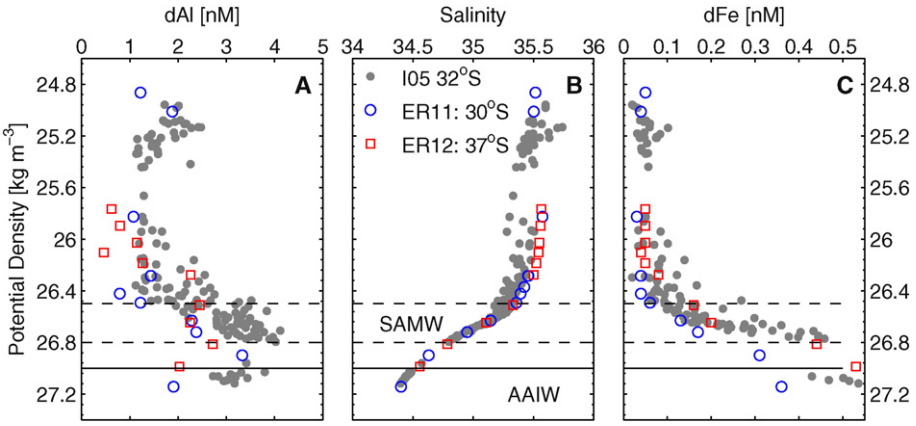

Fig. 6. Data comparison with the GEOTRACES-JAPAN Indian Ocean expedition. See Fig. 1 for station locations. A: dAl [nM], B: salinity, C: dFe [nM]. Gray dots are data from all CLIVAR I05 stations from the SE Indian Ridge to the SW Indian Ridge (~60°E to 75°E). The dashed lines show the density interval of SAMW (26.5–26.8 kg m^{-3}). All data below the full line is considered AAIW (>27 kg m^{-3}).
ER11 and ER12: dAl data from Vu and Sohrin (2013), dFe data from Nishioka et al. (2013).

SISG, we used the modified version of the Measurement of Aluminium for Dust Calculations in Oceanic Waters (MADCOW) described in Grand et al. (2015a). Briefly, this model assumes steady state, only an atmospheric source of Al and calculates total dust deposition (i.e., wet + dry) using the mean dAl concentration in the climatological mixed layer of each I05 station. The depth of the climatological mixed layer is retrieved from the Argo float data compilation of Holte et al. (2010). The model assumes a scavenging residence time of dAl in surface waters of 5 years, a fractional solubility of aerosol Al of 3.6% (derived from all available measurements from the Atlantic and Pacific Oceans) and a constant mass ratio of Al in dust of 8.1% across the transect (Grand et al., 2015a). Our dAl-based total dust deposition fluxes are estimated to have an uncertainty on the order of a factor of 3.5 (Grand et al., 2015a), mainly because of the assumptions of fractional solubility of aerosol Al and mixed layer residence time of dAl, which we assume remain constant along the transect.

4.2.1. dAl based deposition estimates and source regions

Fig. 10 shows our dAl-based estimates of dust deposition along the I05 cruise track overlaid with the annual composite atmospheric model deposition estimates of Mahowald et al. (2005). Although more recent model deposition outputs are presently available (e.g., Mahowald et al., 2011), we use the model data of Mahowald et al. (2005) for consistency with our previous work in the Indian Ocean (Grand et al., 2015a). Our estimates of dust deposition range from 60 to 685 mg m^{-2} yr^{-1}, with higher deposition occurring at the western and eastern ends of the gyre and relatively lower deposition from ~55 to 75°E (Fig. 10; Table 2). The mineralogical composition of aerosols collected at Amsterdam Island in the South Indian Ocean (34°S, 77°E) and during a previous occupation of the I05 cruise track suggest that the principal dust sources impacting the SISG are Australia, South Africa and/or Madagascar (Gaudichet et al., 1989; Witt et al., 2006). Numerical atmospheric models suggest a similar Australian/South African source apportionment across the SISG (Tanaka and Chiba, 2006; Mahowald, 2007; Mahowald et al., 2011). The zonal patterns of total dust deposition inferred from mixed layer dAl along 32°S (Fig. 10) are consistent with the dominance of South African sources impacting the western SISG (<55°E) and Australian aerosols yielding higher deposition in the eastern reaches of the transect (>75°E). From 55 to 75°E, the relatively low dAl-based deposition suggests that air masses influencing this region have a mostly maritime life history and are thus not carrying significant amounts of continental aerosols (Fig. 10). Five-day backward air mass back trajectories run at every other station across the I05 section at altitudes of 10, 500 and 1000 m above sea level (Draxler and Rolph, 2015) show that air masses in the atmospheric marine boundary layer at stations west of ~32.5°E and east of ~105°E briefly passed over South Africa and transited over western Australia within 5-days prior to our sampling, respectively.

4.2.2. Comparison with composite atmospheric model estimates

Our dAl-based estimates of deposition are broadly consistent with composite atmospheric model simulations west of 75°E but not in the

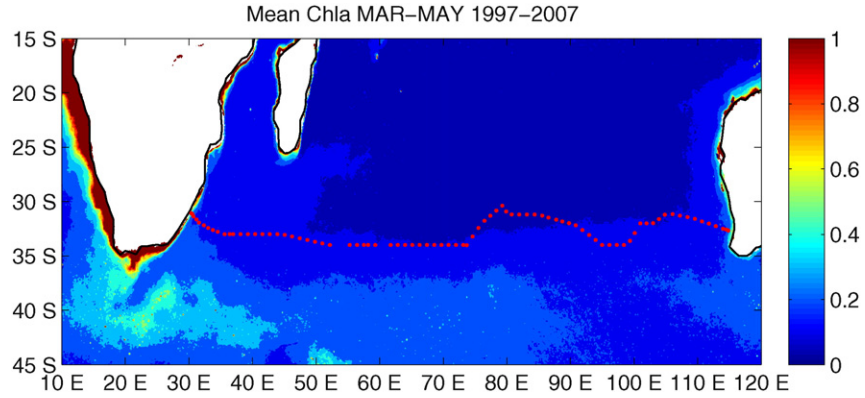

Fig. 7. Mar–Apr–May surface chlorophyll-a levels averaged from 1997 to 2007. The red symbols show the I05 stations. Based on SeaWIFS imagery, units mg m^{-3}.

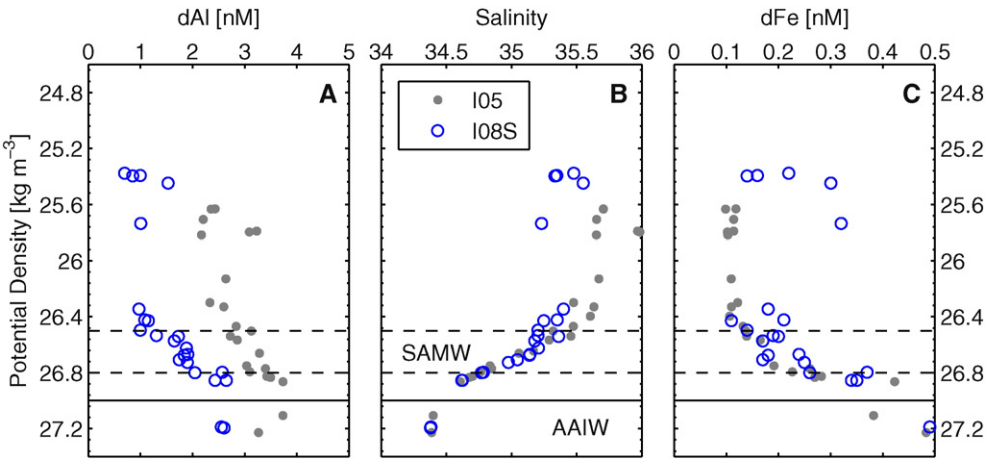

Fig. 8. Data comparison at the I08S/I05 crossover along 95°E. A: dAl [nM], B: salinity, C: dFe [nM]. Gray dots are all the CLIVAR I05 stations from 3 stations along 34°S at 94, 95 and 96°E. The blue dots show data from the I08S cruise (2007) along 95°E at 34.5°S and 33.5°S (Grand et al., 2015b). The dashed lines show the density interval of SAMW. Waters lying below the full line are considered AAIW. Note that the salinity data were analyzed to WOCE precision and accuracy standards on both I05 and I06S.

eastern basin, where our estimates are systematically higher (Fig. 10). In our previous work along a 95°E meridional CLIVAR transect (Grand et al., 2015a), the dAl-based estimates of total deposition were also significantly higher than the model composite of Mahowald et al. (2005), suggesting that models may underestimate the magnitude of Australian dust deposition in the eastern SISG. However, what is perhaps most puzzling are the pronounced latitudinal gradients in our calculated dust deposition occurring west of 75°E (Fig. 10). In particular, the largest discrepancies between our dAl-based estimates and those of atmospheric models occur where the cruise track veered equatorward from ~75°E to 95°E and then from ~100°E to 110°E (Fig. 10). These differences suggest that we sampled the edge of a region in the SISG with significant depositional gradients and appear to confirm that atmospheric models underestimate the magnitude and/or meridional extent of Australian dust deposition in the SISG, consistent with previous findings from the I08S and I09N transects along 95°E (Grand et al., 2015a).

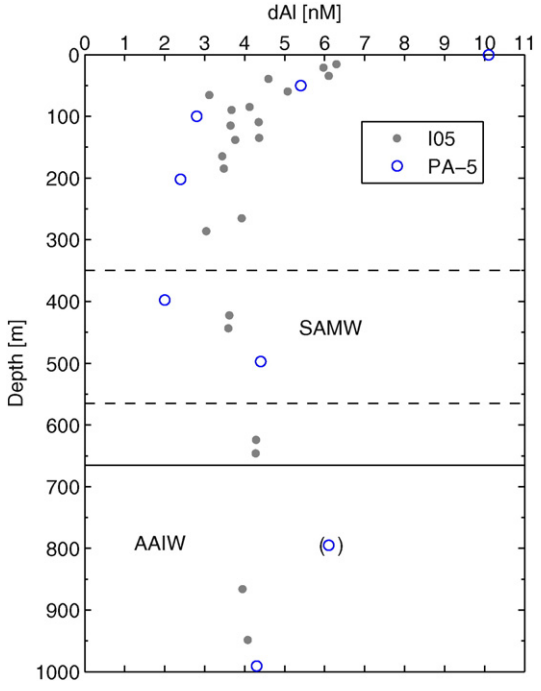

Fig. 9. Data comparison in the eastern Indian Ocean near 110°E. These data are compared with two neighboring I05 stations. See Fig. 1 for station positions. The dashed lines show the approximate depth intervals occupied by SAMW (based on density data from the I05 section at 110°E). Waters below the solid line are AAIW. Note that the data in the blue circle in parenthesis near 800 m from PA-5 is probably contaminated. Since there were no density data available in Obata et al. (2004) work, data are plotted versus depth rather than density.
PA-5 are dAl data (<0.04 μm) from Obata et al. (2004).

There are several factors inherent to the assumptions of the MADCOW model that could produce latitudinal gradients in our deposition estimates east of 75°E (Fig. 10). These include: (1) the advection of dAl-enriched waters from beyond our sampling area at the northernmost stations of the I05 cruise track, (2) latitudinal variations in the fractional solubility of aerosol Al, (3) latitudinal changes in the mixed layer residence time of dAl, and (4) an adventitious combination of all the above parameters. The latitudinal fluctuations in our dAl-based deposition estimates east of 75°E are unlikely to be the result of physical circulation. Indeed, there was no consistent pattern in the LADCP velocities at the northernmost stations of our cruise track suggesting that the higher dAl concentrations observed in these regions (Fig. 11) could be the result of the advection of dAl-enriched waters from elsewhere. The steric height maps of Reid (2003) also suggest that the surface waters along the cruise track originate from the south, where lower surface dAl concentrations are generally found (Grand et al., 2015a). It is also unlikely that variations in the fractional solubility of aerosol Al, which we assume is constant at 3.6% in MADCOW, could produce the pronounced latitudinal gradients in deposition observed along the I05 transect. Indeed, it would be necessary to increase the Al solubility in MADCOW by a factor of about four in order to match the total deposition estimates of Mahowald et al. (2005) in areas where the cruise track veered equatorward (Fig. 10). Considering that the fractional uncertainty ($\pm 2\sigma$) of our mean aerosol Al solubility is ~200% based on all available solubility measurements in the Atlantic and Pacific Oceans (Buck et al., 2010, 2013 as summarized in Grand et al., 2015a), it seems unlikely that fluctuations in the solubility of Al on the order of 400% could occur along the I05 transect. Lastly, it cannot be ruled out that the mixed layer residence time of dAl increases in the northernmost regions of our cruise track. In this regard, we note that we intruded a region characterized with lower surface productivity as the cruise track veered equatorward from 75 to 95°E and again near 110°E (Fig. 7). This observation suggests that scavenging removal rates of dAl at the northernmost stations of our cruise track may be lower, which would increase the residence time of dAl in these waters and produce overestimated dAl-based deposition fluxes when assuming a uniform 5 yr dAl residence time along the transect. However, the

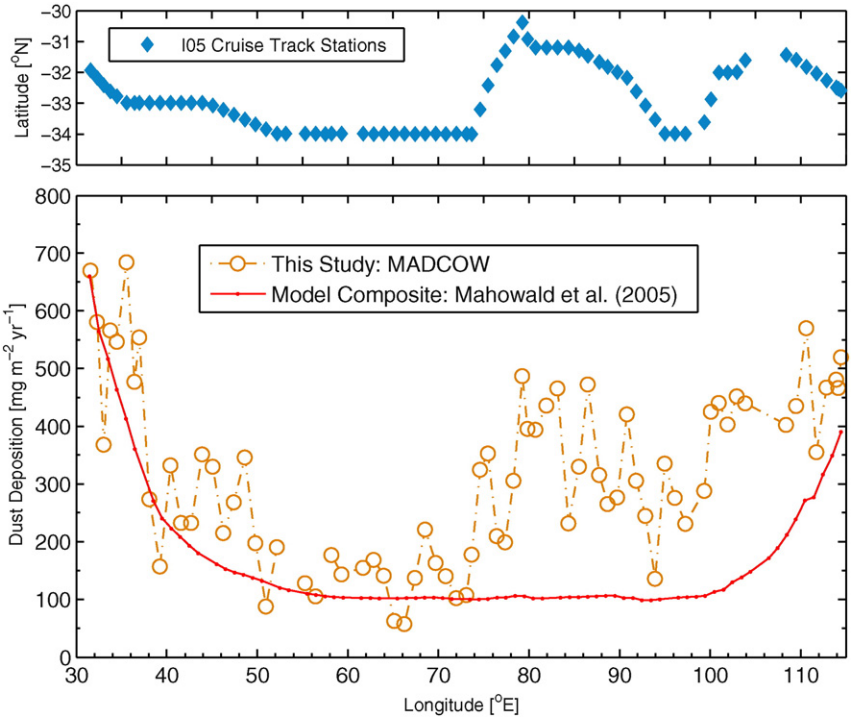

Fig. 10. Dissolved Al-based dust deposition estimates along I05. The composite model deposition estimates of Mahowald et al. (2005) closest to each I05 station are shown by the red line. Note that stations within the Agulhas ($n = 5$) and Leeuwin ($n = 1$) Currents are excluded due to the advection of surface waters of northerly origin. Also excluded are two I05 stations near 97°E and one station near 105°E because of the presence of an eddy bringing deep dAl depleted waters into the mixed layer and an anomalously deep Argo mixed layer.

residence time of dAl would need to be increased by a factor of about four (i.e., about 20 years) as the cruise track headed north from 34°S to 31.5°S (Fig. 10) to match the composite model estimates of Mahowald et al. (2005). Such a sharp change in the scavenging residence time of dAl over such a narrow latitudinal range (i.e., 2.5°) seems rather unlikely in the SISG. Although variations in the above parameters might fortuitously combine to produce the observed latitudinal gradients in deposition shown in Fig. 10, it seems more likely that a large part of the observed gradient in deposition is real, perhaps because we intruded the region where the bulk of Australian dust is being deposited each time the cruise track veered equatorward. The above considerations thus suggest that atmospheric model estimates, which have an uncertainty on the order of a factor of 10 (Mahowald et al., 2005), appear to underestimate total deposition and do not resolve small-scale variations in dust deposition east of 70°E in the SISG (Fig. 10). Interestingly, the observed latitudinal gradients in deposition appear to match the independent gradients we see in N* (discussed in Section 4.2.5), as illustrated by the positive correlation between mean mixed layer N* and mean mixed layer dAl along the I05 transect (Fig. 12).

4.2.3. Dust deposition and mixed layer dFe

The low dFe concentrations in the upper 180 m (0.09 ± 0.05 nM, $n = 426$) of the gyre suggest that dFe inputs from below via convective mixing are negligible considering that the deepest mixed layers observed along the I05 cruise track averaged 80 ± 30 m (mean ± 1σ) since the start of Argo sampling in the Indian Ocean in 2000. Furthermore, mean concentrations of dFe in the mixed layer along the cruise track largely match mixed layer dAl concentrations, suggesting that dust deposition is the dominant source of dFe to the upper layers of the SISG, particularly west of 75°E (Fig. 11). However, there are several regions east of 75°E where mixed layer dAl and dFe are decoupled. Near 97°E, the spike in dFe which is not accompanied by a corresponding dAl spike is most likely due to the presence of a cold core eddy bringing dFe enriched and dAl poor deep waters into the mixed layer (Fig. 11). As mentioned in Section 3.1.2, nitrate and phosphate were elevated in this region (Fig. 4A) while mixed layer salinity and temperature were lower than surrounding stations, consistent with the injection of deeper waters into the mixed layer. It is not clear what causes the decoupling in mixed layer dAl and dFe near 92°E and 102°E (Fig. 11). Since the salinity, temperature and macronutrient data did not reveal any anomalies that could be attributed to inputs from below or waters advected laterally, we surmise that biological uptake of dFe may be responsible for the lower dFe concentrations in these regions.

Table 2
Dust deposition and dFe fluxes along 32°S in the SISG. The numbers given are ranges (min–max) in the western, central and eastern sectors of the SISG.

Longitudinal range	Mineral dust deposition (mg dust m^{-2} yr^{-1})	Aeolian dFe deposition (μmol dFe m^{-2} y^{-1})
Western gyre: 31.6–55°E	90–685	2.6–20
Central gyre: 55–75°E	60–325	1.7–9.5
Eastern gyre: 75–114.5°E	135–570	4.0–17

4.2.4. Aeolian dFe deposition along I05

The magnitude of aeolian dFe deposition across the SISG can be estimated using our dAl-based dust deposition estimates and assuming that dust contains 3.5% Fe (w/w) with a uniform aerosol Fe fractional solubility of 4.6% across the I05 transect (Table 2). The 4.6% fractional solubility of aerosol Fe is the geometric mean of Witt et al. (2010) solubility measurements on aerosol-laden filters collected in the southwest Indian Ocean offshore Madagascar. These data are, to the best of our knowledge, the only published aerosol Fe solubility data for the southern Indian Ocean. We estimate that the deposition and partial dissolution of atmospheric dust may supply 1.7–20 μmol dFe m^{-2} y^{-1} (Fig. 13A, Table 2). Since aerosols originating from South Africa appear to be enriched in Fe relative to the average composition of the continental crust (Witt, 2003; Witt et al., 2006), it is possible that our dFe deposition fluxes at the western end of the transect are underestimated.

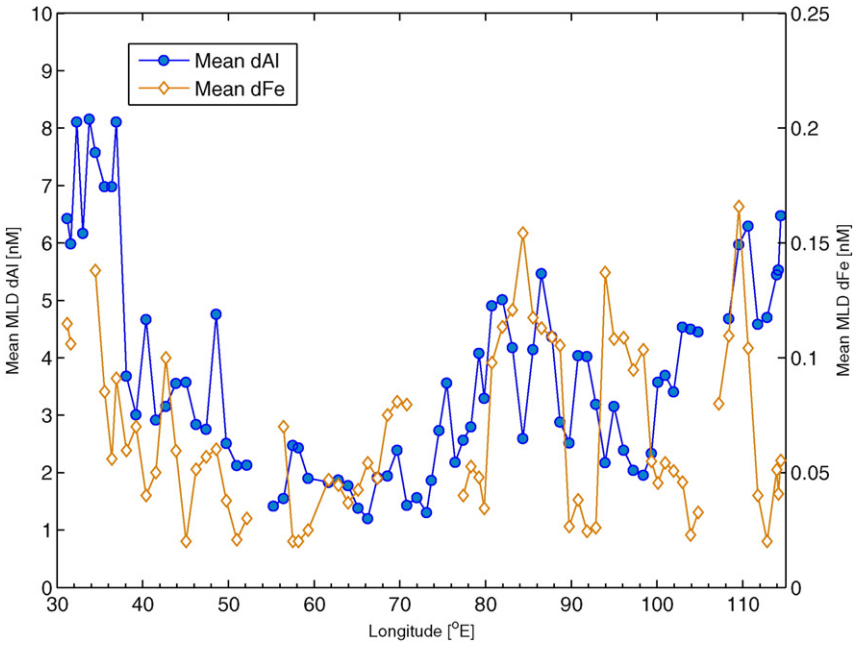

Fig. 11. Mean mixed layer dFe and dAl across the I05 cruise track excluding data from the Agulhas and Leeuwin Current systems. The mixed layer depth (MLD) at each station was calculated using the density criterion of De Boyer Montégut (2004).

Nevertheless, and despite the various uncertainties associated with our approach, our estimates of aeolian dFe deposition from 56 to 67°E (1.7–5.2 μmol dFe m^{-2} yr^{-1}) along 32°S compare very well with the deposition fluxes of Witt et al. (2010) (0.4–5.5 μmol dFe m^{-2} yr^{-1}) calculated within the same longitudinal band at the northern edge of the SISG via shipboard aerosol sampling. Our estimates across the SISG (1.7–20 μmol dFe m^{-2} y^{-1}) are also in good agreement with the modeled soluble Fe deposition data of ~0.6–29 μmol dFe m^{-2} yr^{-1} from the works of Han et al. (2012) and Luo et al. (2008) but are significantly lower than the modeled annual dFe deposition fluxes of 20–-100 μmol dFe m^{-2} yr^{-1} reported by Fan et al. (2006). Note that the model estimates of Fan et al. (2006) also appear to significantly overestimate the magnitude of aeolian dFe deposition to the Indian sector of the Southern Ocean (Grand et al., 2015a).

Using the mean mixed layer depth dFe concentrations and our estimates of dFe deposition at each station along the cruise track, we estimate that the residence time of dFe in the upper layers of the south Indian subtropical gyre with respect to dust deposition is on the order of weeks to months (0.4 ± 0.4 yr, mean ± 1σ). This value is similar to the mean 0.6 yr residence time calculated in the northern reaches of the SISG (Grand et al., 2015a) and also compares well with the ~2 weeks to 5 months range reported for the North Atlantic Ocean (Sarthou et al., 2003; Bergquist and Boyle, 2006; Buck et al., 2010).

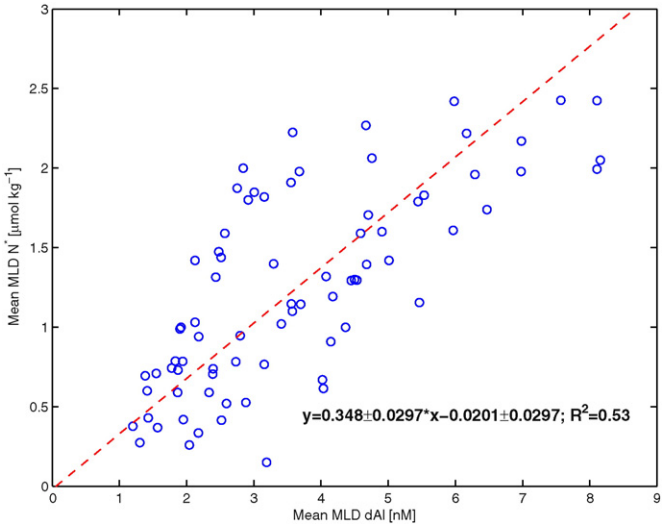

Fig. 12. Model II regression between mean mixed layer N* and dAl along the I05 transect. Note that the stations impacted by the Agulhas and Leeuwin Currents are excluded. The slope and intercept of the equation are given with their respective standard deviations.

4.2.5. Dust deposition and nitrogen fixation across the SISG

Several observational and modeling studies have suggested that the availability of dFe in surface waters of oligotrophic regions may influence the magnitude and location of nitrogen fixation, with important implications for the global oceanic inventory of fixed nitrogen and its response to a changing climate (Falkowski, 1997; Berman-Frank et al., 2001; Moore et al., 2009; Okin et al., 2011; Dutkiewicz et al., 2012; Ward et al., 2013; Shiozaki et al., 2014). Along our 32°S section, the zonal distribution of mean mixed layer N*, an indirect tracer of nitrogen fixation, and the pattern of aeolian dFe deposition inferred from mixed-layer dAl show remarkable similarities (Fig. 13A and B): from west to east, both N* and aeolian dFe deposition decrease from ~30°E to 75°E, show a broad peak near ~70–95°E and then increase east of 100°E until the Australian margin. N* is defined as $N^* = NO_3 - 16PO_4 + 2.9$ μmol kg^{-1}, , and approximates the excess of nitrate in a body of water assuming a constant N:P Redfield ratio of 16:1 during biological uptake and subsequent remineralization of organic matter (Gruber and Sarmiento, 1997; Deutsch et al., 2001). By definition, positive N* values can be interpreted as an excess of nitrate unaccompanied by phosphate, or a loss of phosphate without a stoichiometric nitrate loss.

From a geochemical standpoint, positive N* values could be the result of phosphate removal from the surface layer due to the adsorption of phosphate onto freshly deposited dust particles coated with iron oxyhydroxides, thereby explaining the similarity in the spatial patterns of N* and aeolian dFe inputs and their broad inverse relationship with mixed layer phosphate (Fig. 13). However, phosphate adsorption experiments using Saharan soil and dust samples exposed to Mediterranean seawater showed insignificant adsorption of phosphate onto Saharan soil (Ridame et al., 2003) and dust (<1.3%, Carbo et al., 2005). Positive N* values in the upper layers of the SISG could also result from atmospheric deposition of fixed nitrogen, with enhanced nitrogen

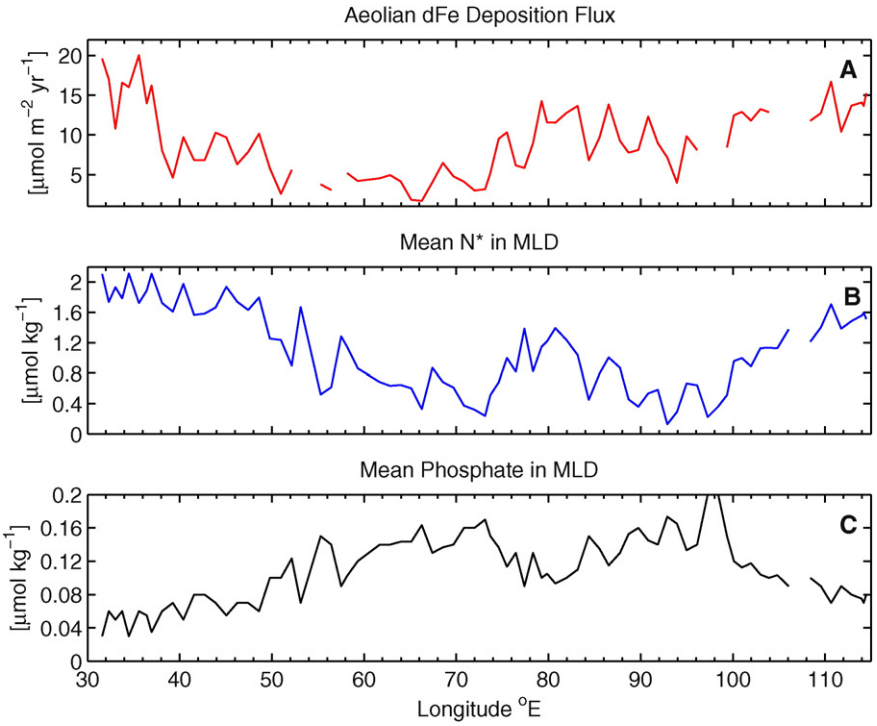

Fig. 13. Aeolian dFe deposition and mean mixed layer (MLD) values of N* and phosphate along the I05 transect. A: Aeolian dFe deposition flux based on our dAl based estimates of dust deposition assuming a 4.6% solubility of aerosol Fe and 3.5% Fe content in dust (w/w). B: Mean N* in the mixed layer calculated using the N* definition ($N^* = NO_3 - 16PO_4 + 2.9\ \mu mol\ kg^{-1}$) of Deutsch et al. (2001). C: Mean mixed layer phosphate.
The depth of the mixed layer at each station was defined using the density criterion of De Boyer Montégut (2004).

deposition likely occurring downwind of industrial and agricultural regions due to fossil fuel combustion and the use and production of fertilizers. However, even an exceptionally large depositional event is unlikely to increase surface concentrations above the threshold that would suppress N_2-fixation (Duce et al., 2008; Zamora et al., 2010). The above considerations suggest that the pattern of N* observed across the mixed layer of the SISG is most likely the result of N-fixation and not the result of abiotic P removal and/or N deposition.

Interestingly, both Gruber and Sarmiento (1997) and Deutsch et al. (2001) observed that the location of nitrogen fixation inferred from N* and model outputs of dust deposition showed similar spatial patterns in the Atlantic and southwest Pacific, respectively. Our data expands this relationship to the SISG using deposition estimates that are based on observations in the upper-ocean rather than atmospheric model outputs. Although the spatial similarities between the distributions of N* and aeolian Fe inputs in the gyre do not constitute proof that nitrogen fixation in the SISG is supported by aeolian dFe inputs, we note that Poulton et al. (2009) observed high numbers of *Trichodesmium* and N_2-fixing diatoms above the Madagascar Ridge near 27°S and east of Madagascar. These observations corroborate the high N* values observed at the western end of our transect (Fig. 13B), where both our estimates and atmospheric models show relatively elevated dust deposition fluxes that originate from the African continent (Fig. 10). In addition, in the Indian Central Water (ICW) along I05 west of 60°E ($\sigma_0 = 26.1$–$26.8\ kg\ m^{-3}$) but excluding the stations influenced by the Agulhas Current on the east African shelf, the slope of Model II regressions between Fe and AOU ($7.3 \pm 0.85\ \mu mol\ mol^{-1}$) and Nitrate and AOU ($0.23 \pm 0.85\ mol\ mol^{-1}$) were 1.8 and 1.5 times higher than that observed along the ICW found along the 95°E eastern Indian Ocean meridional section described in Grand et al. (2015b), respectively. The higher Fe:AOU and Nitrate:AOU ratios observed in the ICW along I05 may reflect the remineralization of Fe rich and N-rich organic material, unlike on the 95°E section where no evidence of nitrogen fixation was observed. Clearly, more observations of the distribution of nitrogen fixing organisms and their activity within the euphotic zone of the SISG are needed to confirm and elucidate the potential impact of aeolian Fe deposition on nitrogen fixing processes in the Indian Ocean.

4.3. The Agulhas Current system and Southwest Indian Subgyre

4.3.1. Particulate and dissolved distributions within the Agulhas Current

The high internal velocities of the Agulhas Current (up to $200\ cm\ s^{-1}$ at the surface and $>10\ cm\ s^{-1}$ at 1000 m depth) have the potential to induce massive sediment erosion, resuspension and transport along the steep and narrow (3–40 km) southeastern African shelf (Flemming, 1981). The impact of the Agulhas Current on sediment dispersal is well illustrated by the particulate Fe (pFe) and Al (pAl) distributions measured at the first five stations of the I05 transect, which show a pronounced decrease with distance from the continental margin with the highest pFe (up to 230 nM) and pAl (up to 690 nM) concentrations measured at the first two stations of the transect, where the highest velocities of the Agulhas Current were observed (Fig. 14). At these stations, the mean pFe:pAl ratio was 0.37 ± 0.05 mol:mol ($n = 20$), within the range of the upper continental crust (0.27, Wedepohl, 1995) and surficial sediments collected at ~2000 m underneath the Agulhas Current near 29.6°S, 32.8°E (0.56, Franzese, 2008).

Although the resuspension of shelf sediments by the Agulhas Current is clearly seen in the particulate distributions, a distinct sedimentary signal is not especially evident in the dAl distributions. For example, the dAl and pAl profiles at the first five I05 stations under the influence of the Agulhas Current do not show similar vertical and horizontal trends (Fig. 14). In particular, the dAl profiles of the first two stations of the I05 section show a typical scavenged like profile, which do not reflect the multiple maxima observed in the pAl distributions (Fig. 14, red and green profiles). In addition, while the pAl profiles exhibit decreasing concentrations with distance from the coast, the second station sampled for dAl on I05 had lower dAl concentrations below 250 m relative to stations further offshore (Fig. 14, green). These considerations suggest that sediment resuspension processes

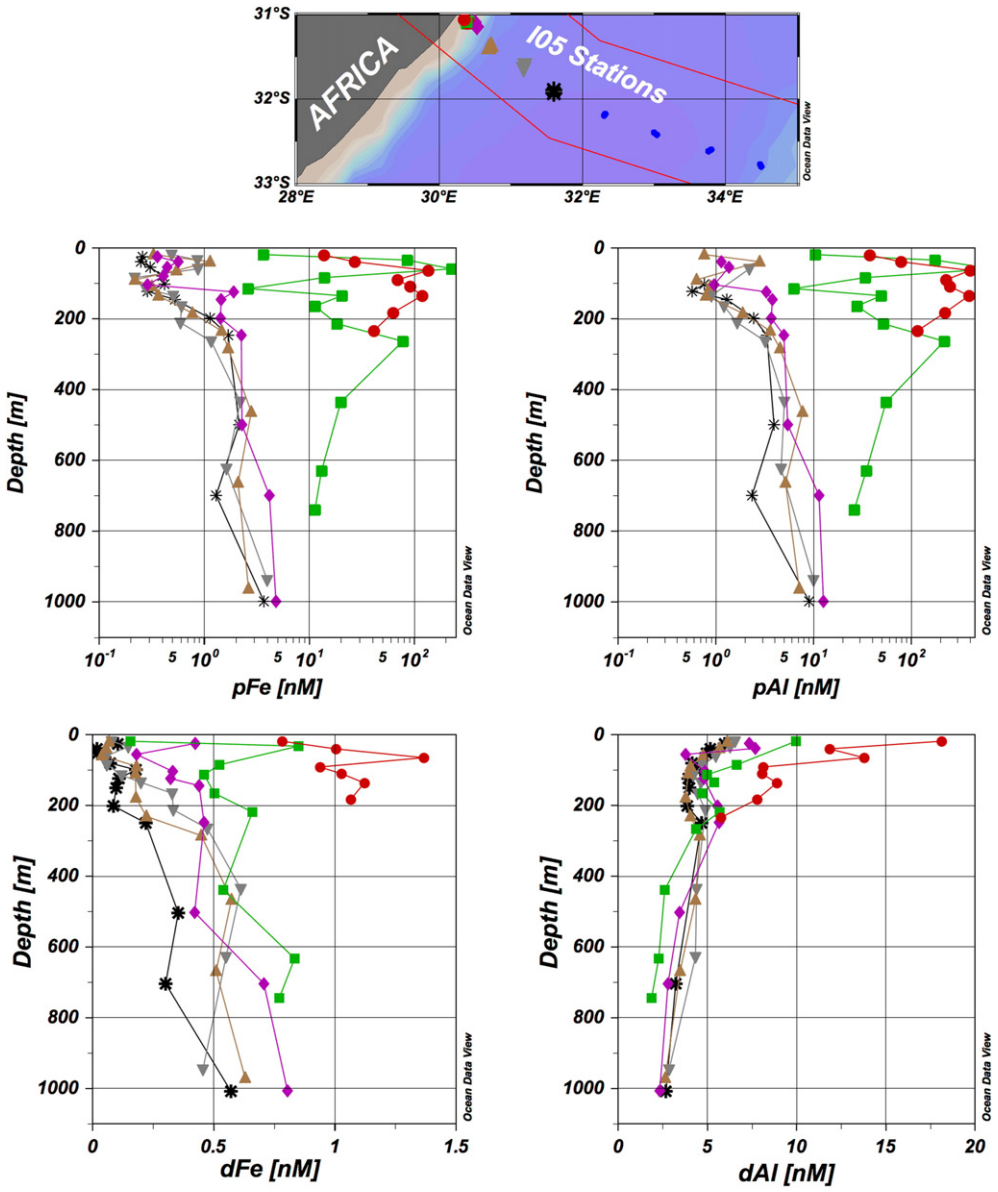

Fig. 14. Particulate and dissolved Fe and Al profiles at the first five stations of the I05 section, which are impacted by the Agulhas Current. Note that the particulate Fe and Al profiles are plotted on a logarithmic scale due to the large zonal concentration gradients.

within the core of the Agulhas Current along the I05 section (i.e., release of pore waters and particle dissolution) have little influence on the distributions of dAl near the African shelf, at least near the I05 section. Rather, the distribution of dAl appears to be dominated by surface dust inputs, scavenging removal and the lateral advection of water masses at depth. In contrast, the dFe and pFe profiles at the first 3 stations of the I05 transect display broadly similar trends, suggesting a greater sedimentary influence on the dFe distributions compared to dAl, perhaps because of the dissolution of Fe-oxyhydroxides coating sediment particles and/or Fe released from organic debris.

The influence of the Agulhas Current on the distribution of dAl near the African shelf can also be investigated by comparing the dAl distributions measured during I06S in February 2008 with the I05 stations located approximately 325 km north and up current of the I06S section (Fig. 1). The dAl concentrations were significantly higher throughout the water column during I06S compared to that observed upstream during I05 (Fig. 15A). For example, in the density interval $\sigma_\theta = 24.5$–26.65 kg m^{-3}, dAl levels were about two times higher on I06S (11.2 ± 1.6 nM, mean $\pm$ 1σ, $n = 22$) than on I05 (5.4 ± 2.21 nM, mean $\pm$ 1σ, $n = 31$) and the difference is significant. Considering the relatively short distance (~325 km) and one-year period that separated the occupation of the I05 and I06S Agulhas crossings as well as the decoupling of the dAl and pAl distributions observed on I05 (see above), the higher dAl concentrations observed in subsurface Agulhas waters on the I06S cruise are more likely the result of physical circulation rather than the result of differing degrees of sediment resuspension along the pathway of the Agulhas Current. One possible explanation for the higher subsurface dAl levels observed on the I06S Agulhas Crossing is that we may have sampled the remnants of a Mozambique Channel eddy embedded in the Agulhas Current during the I06S section but not during I05. This idea is consistent with the lower salinities (Fig. 15B) and higher nitrate concentrations (Fig. 15C) observed in the density interval $\sigma_\theta = 25$–26.2 kg m^{-3} on I06S relative to I05, considering that Mozambique Channel eddies supply waters with elevated nitrate concentrations to the headwaters of the Agulhas Current that are inherited from the tropical northwestern Indian Ocean (Swart et al., 2010). More observations along the pathway of the Agulhas Current are needed to determine and quantify the processes that

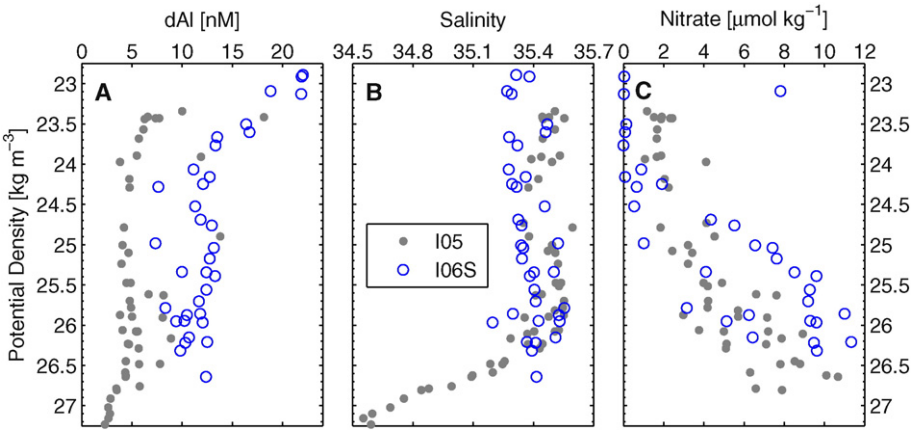

Fig. 15. Data comparison at the I05 and I06S Agulhas Current crossings. A: dAl [nM], B: salinity, C: nitrate [μmol kg^{-1}]. The I05 and I06S Agulhas crossings were sampled one year apart and are located ~325 km from each other. Note that the salinity and nitrate data were analyzed to WOCE precision and accuracy standards on both I05 and I06S. Thus the differences in salinity and nitrate concentrations between I05 and I06S are real and not the result of an analytical offset.

could deliver dAl and dFe enriched waters to the Agulhas retroflection region and Agulhas Return Current. Such data would be particularly useful to determine the role of bioactive trace elements in sustaining the relatively elevated productivity that coincides with the path of the Agulhas retroflection and Agulhas Return Current west of 40°E (Fig. 7).

4.3.2. Elevated dAl in the Southwest Indian Subgyre

We now focus on the subsurface region (~100–700 m) of elevated dAl (>4 nM), which extends from the African margin and terminates near the Madagascar Ridge near 45–50°E (Fig. 3C). This region also coincides with elevated subsurface dFe levels, particularly at ~100–400 m relative to regions east of the Madagascar Ridge (Fig. 3D). The subsurface waters occupying the water column west of Madagascar ridge are part of the recirculation cell of the Southwest Indian Subgyre, as illustrated by lower oxygen levels relative to the SAMW lying to the east (Fig. 3B). Considering that about 60% of the upper 1000 m flow of the Agulhas Current appears to be returned in the Southwest Indian Subgyre along the advective pathway of the Agulhas Return Current (Lutjeharms, 2006), any geochemical imprints acquired and/or transported with the Agulhas Current may be transferred, albeit in an eroded form, into the Southwest Indian Subgyre.

Table 3 compares the mean dAl concentrations between the density intervals 25.75–26.75 kg m^{-3} west of Madagascar Ridge but outside of the Agulhas Current from I05 with that observed within the same density intervals at 2 stations near the Agulhas Return Current during I06S. The concentrations of dAl were significantly higher within the Agulhas Return Current compared to that observed in the Southwest Indian Subgyre during I05 in both density intervals listed in Table 3 (Mann–Whitney U-test, $p < 0.01$), suggesting that the recirculation of dAl enriched Agulhas Return Current waters into the Southwest Indian Subgyre can sustain the elevated dAl concentrations observed along 32°S west of Madagascar Ridge. The termination of the region of elevated dAl near the Madagascar ridge (45–50°E) is consistent with hydrographic observations along the path of the Agulhas Return Current, which suggest that the major leakage of the Agulhas Return Current into the Southwest Indian Subgyre occurs west of 45–50°E (Sparrow et al., 1996; Lutjeharms and Ansorge, 2001; Lutjeharms, 2006). Interestingly, the dAl concentrations decreased by about 40% from the Agulhas Return Current to 32°S in the density range 25.75–26.75 kg m^{-3} and below 26.75 kg m^{-3}, suggesting that dAl-rich Agulhas Return Current waters within these two density intervals are subjected to the same degree of mixing and scavenging dAl removal during their northward transit (Table 3).

Table 3
Dissolved Al (nM) in the Agulhas Return Current (I06S) and Southwest Indian sub-gyre (I05). The data from the Southwest Indian sub-gyre are from 32.3°E to 45°E along I05 and exclude data from the Agulhas Current system.

Density range	Agulhas Return Current	I05 SW Indian sub-gyre
$\sigma_\theta = 25.75–26.75$ kg m^{-3}	7.2 ± 0.8 nM ($n = 7$)	4.7 ± 0.6 nM ($n = 54$)
$\sigma_\theta > 26.75$ kg m^{-3}	5.8 ± 0.9 nM ($n = 3$)	3.4 ± 0.3 nM ($n = 14$)

5. Conclusions

The distributions of dFe and dAl (<0.45 μm) in the South Indian Subtropical Gyre are primarily impacted by mineral dust deposition and the large-scale circulation patterns of the gyre. The influence of the gyre circulation was particularly evident for dAl, considering that the majority of the subsurface features in the dAl distribution are consistent with the accepted dynamics and circulation pathways of water masses occupying the main thermocline of the South Indian Subtropical Gyre. Using data from the meridional I06S transect along 30°E, we show that the relatively elevated subsurface dAl values west of the Madagascar Ridge along 32°S can be sustained by leakage of dAl-rich waters from the Agulhas Return Current into the Southwest Indian Subgyre. The termination of this region of elevated dAl in the vicinity of the Madagascar Ridge (45–50°E) corroborates the notion that most of the leakage from the Agulhas Return Current into the Southwest Indian Subgyre likely occurs west of about 50°E and considerably decreases beyond this longitude. Further east near 80°E, low subsurface dAl concentrations along 32°S appear to coincide with the longitude where Subantarctic Mode Waters formed north of Kerguelen Island are injected into the gyre. Near the southeast African continental margin, the particulate Al and Fe distributions confirm the role of the Agulhas in sediment resuspension and dispersal. However, the effect of sediment resuspension was not clearly replicated in the dissolved Al distributions, suggesting that sediment resuspension plays a minor role in setting the elevated dAl concentrations observed within the core of the Agulhas Current along I05 and I06S.

The dominant source of dAl and dFe to the mixed layer of the South Indian Subtropical Gyre is the deposition and partial dissolution of mineral dust. Using mean dAl concentrations in the climatological mixed layer and a simple steady state model, we calculate that the total dust deposition fluxes (i.e., wet + dry) impacting the south Indian gyre range from 60 to 685 mg (dust) m^{-2} yr^{-1}, with higher deposition occurring at the western (<40°E) and eastern (>70°E) margins, where dust most likely originates from the South African and Australian landmasses, respectively. We find that our estimates of dust deposition are in reasonable agreement with composite model estimates, except in the northeastern reaches of the gyre, where models appear to underestimate the magnitude of deposition. Using available measurements of

the fractional solubility of aerosol Fe from the south Indian subtropical gyre, we estimate that dust deposition could supply 1.7–20 μmol dFe m^{-2} y^{-1} to the mixed layer and that the steady state residence time of dFe in the upper layers of the south Indian gyre is generally less than 6 months. Interestingly, the zonal patterns of deposition and those of N*, an indirect geochemical tracer of nitrogen fixation, show remarkable similarities in the upper layers of the South Indian Subtropical Gyre. This observation, along with the elevated Fe:AOU and Nitrate:AOU ratios in Indian Central Water west of 60°E, lends support to the assertion that iron availability may regulate diazotrophic activity in oligotrophic subtropical waters and warrants additional observations of nitrogen fixation rates to better constrain the importance of nitrogen fixation across the South Indian Subtropical Gyre and its relationship to aeolian delivery of dFe.

Taken together, the CLIVAR dFe and dAl data from the Indian Ocean suggest that the prime requirements to develop accurate model simulations of the distributions of dAl and dFe in the main thermocline are to first ensure that the model can accurately reproduce the main circulation features and water mass pathways and is forced with estimates of dust deposition that are validated against field observations and/or other indirect estimates. Although the remineralization of sinking organic matter is clearly an important process impacting the subsurface distribution of dissolved Fe, our data from three high-resolution meridional CLIVAR transects (I08S, I08N and I06S) and one zonal transect (I05) across of variety of biogeochemical regimes in the Indian Ocean show no evidence for biological remineralization of dissolved Al in the main thermocline of the Indian Ocean.

Supplementary data to this article can be found online at http://dx.doi.org/10.1016/j.marchem.2015.08.002.

Acknowledgments

We thank the crew and captains of the *R/V Roger Revelle* and chief scientists Jim Swift (I05) and Kevin Speer (I06S) for their tremendous technical and logistical support, particularly on I06S when we were faced with many technical difficulties following the failed delivery of our hydraulic winch and loss of our CTD rosette. We also acknowledge Kati Gosnell and William Hiscock for their help during the seagoing part of this project as well as Yoshiki Sohrin and Natalie Mahowald for sharing their data and two anonymous reviewers for their comments. The ICP-MS analyses reported here were performed at the National High Magnetic Field Laboratory, which is supported by the National Science Foundation cooperative agreement no. DMR-1157490 and the State of Florida. This work was funded by NSF-OCE-0649584 to CIM, NSF-OCE-0550317 and 0649639 to WML and NSF-OCE-1260376 to JAR. This is SOEST contribution number 9484 and JISAO and PMEL publications #2413 and #4290, respectively.

References

Anderson, R., Mawji, E., Cutter, G., Measures, C.I., Jeandel, C., 2014. GEOTRACES: changing the way we explore ocean chemistry. Oceanography 27 (1), 50–61. http://dx.doi.org/10.5670/oceanog.2014.07.

Barrett, P.M., Resing, J.A., Buck, N.J., Buck, C.S., Landing, W.M., Measures, C.I., 2012. The trace element composition of suspended particulate matter in the upper 1000 m of the eastern North Atlantic Ocean: A16N. Mar. Chem. 142–144, 41–53. http://dx.doi.org/10.1016/j.marchem.2012.07.006.

Barrett, P.M., Resing, J.A., Buck, N.J., Landing, W.M., Morton, P.L., Shelley, R.U., 2015. Changes in the distribution of Al and particulate Fe along A16N in the eastern North Atlantic Ocean between 2003 and 2013: implications for changes in dust deposition. Mar. Chem. http://dx.doi.org/10.1016/j.marchem.2015.02.009.

Beal, L.M., Bryden, H.L., 1999. The velocity and vorticity structure of the Agulhas. J. Geophys. Res. 104 (C3), 5151–5176. http://dx.doi.org/10.1029/1998JC900056.

Bergquist, B.A., Boyle, E.A., 2006. Dissolved iron in the tropical and subtropical Atlantic Ocean. Glob. Biogeochem. Cycles 20 (GB1015), 1–14. http://dx.doi.org/10.1029/2005GB002505.

Berman-Frank, I., Cullen, J.T., Shaked, Y., Sherrell, R.M., Falkowski, P.G., 2001. Iron availability, cellular iron quotas, and nitrogen fixation in *Trichodesmium*. Limnol. Oceanogr. 46 (6), 1249–1260. http://dx.doi.org/10.4319/lo.2001.46.6.1249.

Boyd, P., et al., 2007. Mesoscale iron enrichment experiments 1993–2005: synthesis and future directions. Science 315, 612–617. http://dx.doi.org/10.1126/science.1131669.

Bruland, K.W., Lohan, M.C., 2003. Controls of trace metals in seawater. In: Elderfield, K.K., Holland, H., Turekian, D. (Eds.), Treatise on Geochemistry, pp. 23–47.

Buck, C.S., Landing, W.M., Resing, J.A., Measures, C.I., 2010. The solubility and deposition of aerosol Fe and other trace elements in the North Atlantic Ocean: observations from the A16N CLIVAR/CO_2 repeat hydrography section. Mar. Chem. 120, 57–70. http://dx.doi.org/10.1016/j.marchem.2008.08.003.

Buck, C.S., Landing, W.M., Resing, J.A., 2013. Pacific Ocean aerosols: deposition and solubility of iron, aluminum, and other trace elements. Mar. Chem. 157, 117–130. http://dx.doi.org/10.1016/j.marchem.2013.09.005.

Carbo, P., Krom, M.D., Homoky, W.B., Benning, L.G., Herut, B., 2005. Impact of atmospheric deposition on N and P geochemistry in the southeastern Levantine basin. Deep-Sea Res. II Top. Stud. Oceanogr. 52 (22–23), 3041–3053. http://dx.doi.org/10.1016/j.dsr2.2005.08.014.

Chin, M., et al., 2014. Multi-decadal aerosol variations from 1980 to 2009: a perspective from observations and a global model. Atmos. Chem. Phys. 14 (7), 3657–3690. http://dx.doi.org/10.5194/acp-14-3657-2014.

Dammshäuser, A., Croot, P.L., 2012. Low colloidal associations of aluminium and titanium in surface waters of the tropical Atlantic. Geochim. Cosmochim. Acta 96, 304–318. http://dx.doi.org/10.1016/j.gca.2012.07.032.

De Baar, H.J.W., et al., 2005. Synthesis of iron fertilization experiments: from the iron age in the age of enlightenment. J. Geophys. Res. C: Oceans 110 (C09S16), 1–24. http://dx.doi.org/10.1029/2004JC002601.

De Boyer Montégut, C., 2004. Mixed layer depth over the global ocean: an examination of profile data and a profile-based climatology. J. Geophys. Res. 109 (C12). http://dx.doi.org/10.1029/2004JC002378 (C12003).

Deutsch, C., Gruber, N., Key, R.M., Sarmiento, J.L., Ganachaud, A., 2001. Denitrification and N_2 fixation in the Pacific Ocean. Glob. Biogeochem. Cycles 15 (2), 483–506. http://dx.doi.org/10.1029/2000GB001291.

Domingues, C.M., Maltrud, M.E., Wijffels, S.E., Church, J.A., Tomczak, M., 2007. Simulated Lagrangian pathways between the Leeuwin Current System and the upper-ocean circulation of the southeast Indian Ocean. Deep-Sea Res. II Top. Stud. Oceanogr. 54 (8–10), 797–817. http://dx.doi.org/10.1016/j.dsr2.2006.10.003.

Donohue, K.A., Toole, J.M., 2003. A near-synoptic survey of the Southwest Indian Ocean. Deep-Sea Res. II Top. Stud. Oceanogr. 50 (12–13), 1893–1931. http://dx.doi.org/10.1016/S0967-0645(03)00039-0.

Draxler, R.R., Rolph, G.D., 2015. HYSPLIT (HYbrid Single-Particle Lagrangian Integrated Trajectory) Model access via NOAA ARL READY Website. NOAA Air Resources Laboratory, Silver Spring, MD Available from: http://ready.arl.noaa.gov/HYSPLIT.php.

Duce, R.A., et al., 2008. Impacts of atmospheric anthropogenic nitrogen on the open ocean. Science 320 (5878), 893–897. http://dx.doi.org/10.1126/science.1150369.

Dutkiewicz, S., Ward, B.A., Monteiro, F., Follows, M.J., 2012. Interconnection of nitrogen fixers and iron in the Pacific Ocean: theory and numerical simulations. Glob. Biogeochem. Cycles 26 (1). http://dx.doi.org/10.1029/2011GB004039.

Falkowski, P.G., 1997. Evolution of the nitrogen cycle and its influence on biological sequestration of CO_2 in the ocean. Nature 387, 272–274. http://dx.doi.org/10.1038/387272a0.

Fan, S., Moxim, W.J., Levy, H.L., 2006. Aeolian input of bioavailable iron to the ocean. Geophys. Res. Lett. 33 (L07602), 2–5. http://dx.doi.org/10.1029/2005GL024852.

Fine, R.A., 1993. Circulation of Antarctic intermediate water in the South Indian Ocean. Deep-Sea Res. I Oceanogr. Res. Pap. 40 (10), 2021–2042. http://dx.doi.org/10.1016/0967-0637(93)90043-3.

Flemming, B.W., 1981. Factors controlling shelf sediment dispersal along the southeast African continental margin. Mar. Geol. 42, 259–277.

Franzese, A. (2008), Paleoceanography of the Agulhas Current and Retroflection determined by radiogenic isotopes in deep-sea sediments. Unpublished Ph.D Dissertation, 289 pp., Columbia University, USA.

Gaudichet, A., Lefevre, R., Gaudry, A., Ardouin, B., Lambert, G., 1989. Mineralogical composition of aerosols at Amsterdam Island. Tellus B 41B (3), 344–352. http://dx.doi.org/10.1111/j.1600-0889.1989.tb00313.x.

Grand, M., Buck, C., Landing, W., Measures, C., Hatta, M., Hiscock, W., Brown, M., Resing, J., 2014. Quantifying the impact of atmospheric deposition on the biogeochemistry of Fe and Al in the upper ocean: a decade of collaboration with the US CLIVAR-CO_2 Repeat Hydrography Program. Oceanography 27 (1), 62–65. http://dx.doi.org/10.5670/oceanog.2014.08.

Grand, M.M., Measures, C.I., Hatta, M., Hiscock, W.T., Buck, C.S., Landing, W.M., 2015a. Dust deposition in the eastern Indian Ocean: the ocean perspective from Antarctica to the Bay of Bengal. Glob. Biogeochem. Cycles 29 (3). http://dx.doi.org/10.1002/2014GB004898.

Grand, M.M., Measures, C.I., Hatta, M., Hiscock, W.T., Landing, W.M., Morton, P.L., Buck, C.S., Barrett, P.M., Resing, J.A., 2015b. Dissolved Fe and Al in the upper 1000 m of the eastern Indian Ocean: a high-resolution transect along 95°E from the Antarctic margin to the Bay of Bengal. Glob. Biogeochem. Cycles 29 (3). http://dx.doi.org/10.1002/2014GB004920.

Gruber, N., Sarmiento, J.L., 1997. Global patterns of marine nitrogen fixation and denitrification. Glob. Biogeochem. Cycles 11 (2), 235–266. http://dx.doi.org/10.1029/97GB00077.

Han, Q., Zender, C.S., Moore, J.K., Buck, C.S., Chen, Y., Johansen, A., Measures, C.I., 2012. Global estimates of mineral dust aerosol iron and aluminum solubility that account for particle size using diffusion-controlled and surface-area-controlled approximations. Glob. Biogeochem. Cycles 26 (2). http://dx.doi.org/10.1029/2011GB004186.

Hatta, M., Measures, C., Wu, J., Fitzsimmons, J., Morton, P., 2014. Overview: dissolved Fe and Mn concentrations in the North Atlantic during GEOTRACES 2010/2011 cruises. Deep-Sea Res. II http://dx.doi.org/10.1016/j/dsr2.2014.07.005.

Holte, J., Gilson, J., Talley, L., Roemmich, D., 2010. Argo Mixed Layers, Scripps Institution of Oceanography/UCSD. Available from:, http://mixedlayer.ucsd.edu (Accessed 15 October 2013).
Jickells, T.D., et al., 2005. Global iron connections between desert dust, ocean biogeochemistry, and climate. Science 308, 67–71. http://dx.doi.org/10.1126/science.1105959.
Klunder, M.B., Laan, P., Middag, R., De Baar, H.J.W., Ooijen, J.V., 2011. Dissolved iron in the Southern Ocean (Atlantic sector). Deep-Sea Res. II Top. Stud. Oceanogr. 58, 2678–2694. http://dx.doi.org/10.1016/j.dsr2.2010.10.042.
Klunder, M.B., Bauch, D., Laan, P., de Baar, H.J.W., van Heuven, S., Ober, S., 2012. Dissolved iron in the Arctic shelf seas and surface waters of the central Arctic Ocean: impact of Arctic river water and ice-melt. J. Geophys. Res. 117 (C1). http://dx.doi.org/10.1029/2011JC007133 (C01027).
Klunder, M.B., Laan, P., De Baar, H.J.W., Middag, R., Neven, I., Van Ooijen, J., 2014. Dissolved Fe across the Weddell Sea and Drake Passage: impact of DFe on nutrient uptake. Biogeosciences 11 (3), 651–669. http://dx.doi.org/10.5194/bg-11-651-2014.
Koch-Larrouy, A., Morrow, R., Penduff, T., Juza, M., 2010. Origin and mechanism of Subantarctic Mode Water formation and transformation in the Southern Indian Ocean. Ocean Dyn. 60 (3), 563–583. http://dx.doi.org/10.1007/s10236-010-0276-4.
Luo, C., Mahowald, N., Bond, T., Chuang, P.Y., Artaxo, P., Siefert, R., Chen, Y., Schauer, J., 2008. Combustion iron distribution and deposition. Glob. Biogeochem. Cycles 22 (1). http://dx.doi.org/10.1029/2007GB002964.
Lutjeharms, J.R., 2006. The Agulhas Current. Springer, Berlin (ISBN103540, Ed.).
Lutjeharms, J.R.E., Ansorge, I.J., 2001. The Agulhas Return Current. J. Mar. Syst. 115–138. http://dx.doi.org/10.1016/S0924-7963(01)00041-0.
Mahowald, N.M., 2007. Anthropocene changes in desert area: sensitivity to climate model predictions. Geophys. Res. Lett. 34 (18). http://dx.doi.org/10.1029/2007GL030472 (L18817).
Mahowald, N.M., Baker, A.R., Bergametti, G., Brooks, N., Duce, R.A., Jickells, T.D., Kubilay, N., Prospero, J.M., Tegen, I., 2005. Atmospheric global dust cycle and iron inputs to the ocean. Glob. Biogeochem. Cycles 19. http://dx.doi.org/10.1029/2004GB002402.
Mahowald, N., Albani, S., Engelstaedter, S., Winckler, G., Goman, M., 2011. Model insight into glacial–interglacial paleodust records. Quat. Sci. Rev. 30 (7–8), 832–854. http://dx.doi.org/10.1016/j.quascirev.2010.09.007.
Maring, H.B., Duce, R.A., 1987. The impact of atmospheric aerosols on trace metal chemistry in open ocean surface seawater, 1. Aluminum. Earth Planet. Sci. Lett. 84 (4), 381–392. http://dx.doi.org/10.1016/0012-821X(87)90003-3.
McDonagh, E.L., Bryden, H.L., King, B.A., Sanders, R.J., Cunningham, S.A., Marsh, R., 2005. Decadal changes in the South Indian Ocean thermocline. J. Clim. 18 (10), 1575–1590. http://dx.doi.org/10.1175/JCLI3350.1.
Measures, C., Brown, E., 1996. Estimating dust input to the Atlantic ocean using surface water aluminium concentrations. In: Guerzoni, S., Chester, R. (Eds.), The Impact of Desert Dust Across the Mediterranean. Kluwer Academic Publishers, Netherlands, pp. 301–311.
Measures, C.I., Edmond, J.M., 1990. Aluminium in the South Atlantic: steady state distribution of a short residence time element. J. Geophys. Res. 95 (C4), 5331. http://dx.doi.org/10.1029/JC095iC04p05331.
Measures, C., Vink, S., 2000. On the use of dissolved aluminium in surface waters to estimate dust deposition to the ocean. Glob. Biogeochem. Cycles 14 (1), 317–327. http://dx.doi.org/10.1029/1999GB001188.
Measures, C.I., Yuan, J., Resing, J.A., 1995. Determination of iron in seawater by flow injection analysis using in-line preconcentration and spectrophotometric detection. Mar. Chem. 50, 1–10. http://dx.doi.org/10.1016/0304-4203(95)00022-J.
Measures, C.I., Landing, W.M., Brown, M.T., Buck, C.S., 2008a. A commercially available rosette system for trace metal clean sampling. Limnol. Oceanogr. Methods 6, 384–394. http://dx.doi.org/10.4319/lom.2008.6.384.
Measures, C.I., Landing, W.M., Brown, M.T., Buck, C.S., 2008b. High-resolution Al and Fe data from the Atlantic Ocean CLIVAR-CO_2 Repeat Hydrography A16N transect: extensive linkages between atmospheric dust and upper ocean geochemistry. Glob. Biogeochem. Cycles 22 (GB1005), 101029. http://dx.doi.org/10.1029/2007GB003042.
Measures, C.I., Sato, T., Vink, S., Howell, S., Li, Y.H., 2010. The fractional solubility of aluminium from mineral aerosols collected in Hawaii and implications for atmospheric deposition of biogeochemically important trace elements. Mar. Chem. 120 (1–4), 144–153. http://dx.doi.org/10.1016/j.marchem.2009.01.014.
Measures, C.I., Hatta, M., Fitzsimmons, J., Morton, P., 2014. Dissolved Al in the zonal N Atlantic section of the US GEOTRACES 2010/2011 cruises. Deep-Sea Res. II http://dx.doi.org/10.1016/j.dsr2.2014.07.006.
Middag, R., de Baar, H., Laan, P., Bakker, K., 2009. Dissolved aluminium and the silicon cycle in the Arctic Ocean. Mar. Chem. 115, 176–195. http://dx.doi.org/10.1016/j.marchem.2009.08.002.
Middag, R., de Baar, H.J.W., Laan, P., Huhn, O., 2012. The effects of continental margins and water mass circulation on the distribution of dissolved aluminum and manganese in Drake Passage. J. Geophys. Res. 117 (C1). http://dx.doi.org/10.1029/2011JC007434 (C01019).
Middag, R., de Baar, H.J.W., Klunder, M.B., Laan, P., 2013. Fluxes of dissolved aluminum and manganese to the Weddell Sea and indications for manganese co-limitation. Limnol. Oceanogr. 58 (1), 287–300. http://dx.doi.org/10.4319/lo.2013.58.1.0287.
Mills, M.M., Ridame, C., Davey, M., La Roche, J., Geider, R.J., 2004. Iron and phosphorus co-limit nitrogen fixation in the eastern tropical North Atlantic. Nature 429, 292–294. http://dx.doi.org/10.1038/nature02550 (May).
Milne, A., Landing, W., Bizimis, M., Morton, P., 2010. Determination of Mn, Fe, Co, Ni, Cu, Zn, Cd and Pb in seawater using high resolution magnetic sector inductively coupled mass spectrometry (HR-ICP-MS). Anal. Chim. Acta 665 (2), 200–207. http://dx.doi.org/10.1016/j.aca.2010.03.027.
Moore, J.K., Doney, S.C., 2007. Iron availability limits the ocean nitrogen inventory stabilizing feedbacks between marine denitrification and nitrogen fixation. Glob. Biogeochem. Cycles 21 (2). http://dx.doi.org/10.1029/2006GB002762.
Moore, C., et al., 2009. Large-scale distribution of Atlantic nitrogen fixation controlled by iron availability. Nat. Geosci. 2 (12), 867–871. http://dx.doi.org/10.1038/ngeo667.
Moran, S.B., Moore, R.M., 1989. The distribution of colloidal aluminum and organic carbon in coastal and open ocean waters off Nova Scotia. Geochim. Cosmochim. Acta 53 (10), 2519–2527. http://dx.doi.org/10.1016/0016-7037(89)90125-7.
Moran, S., Moore, R., 1992. Kinetics of the removal of dissolved aluminium by diatoms in seawater: a comparison with thorium. Geochim. Cosmochim. Acta 56, 3365–3374. http://dx.doi.org/10.1016/0016-7037(92)90384-U.
Nishioka, J., Obata, H., Tsumune, D., 2013. Evidence of an extensive spread of hydrothermal dissolved iron in the Indian Ocean. Earth Planet. Sci. Lett. 361, 26–33. http://dx.doi.org/10.1016/j.epsl.2012.11.040.
Obata, H., Nozaki, Y., Alibo, D.S., Yamamoto, Y., 2004. Dissolved Al, In, and Ce in the eastern Indian Ocean and the Southeast Asian Seas in comparison with the radionuclides ^{210}Pb and ^{210}Po. Geochim. Cosmochim. Acta 68 (5), 1035–1048. http://dx.doi.org/10.1016/j.gca.2003.07.021.
Okin, G.S., et al., 2011. Impacts of atmospheric nutrient deposition on marine productivity: roles of nitrogen, phosphorus, and iron. Glob. Biogeochem. Cycles 25 (2). http://dx.doi.org/10.1029/2010GB003858.
Orians, K.J., Bruland, K.W., 1985. Dissolved aluminium in the central North Pacific. Nature 316 (6027), 427–429. http://dx.doi.org/10.1038/316427a0.
Poulton, A.J., Stinchcombe, M.C., Quartly, G.D., 2009. High numbers of *Trichodesmium* and diazotrophic diatoms in the southwest Indian Ocean. Geophys. Res. Lett. 36 (15). http://dx.doi.org/10.1029/2009GL039719.
Reid, J.L., 2003. On the total geostrophic circulation of the Indian Ocean: flow patterns, tracers, and transports. Prog. Oceanogr. 56 (1), 137–186. http://dx.doi.org/10.1016/S0079-6611(02)00141-6.
Reitmeyer, R., Powell, R.T., Landing, W.M., Measures, C.I., 1996. Colloidal aluminum and iron in seawater: an intercomparison between various cross-flow ultrafiltration systems. Mar. Chem. 55 (1–2), 75–91. http://dx.doi.org/10.1016/S0304-4203(96)00049-7.
Resing, J., Measures, C.I., 1994. Fluorometric determination of Al in seawater by flow injection analysis with in-line preconcentration. Anal. Chem. 66, 4105–4111. http://dx.doi.org/10.1021/ac00094a039.
Ridame, C., Moutin, T., Guieu, C., 2003. Does phosphate adsorption onto Saharan dust explain the unusual N/P ratio in the Mediterranean Sea? Oceanol. Acta 26 (5–6), 629–634. http://dx.doi.org/10.1016/S0399-1784(03)00061-6.
Rijkenberg, M.J.A., Middag, R., Laan, P., Gerringa, L.J.A., van Aken, H.M., Schoemann, V., de Jong, J.T.M., de Baar, H.J.W., 2014. The distribution of dissolved iron in the west Atlantic Ocean. PLoS One 9 (6), e101323. http://dx.doi.org/10.1371/journal.pone.0101323.
Sarthou, G., et al., 2003. Atmospheric iron deposition and sea-surface dissolved iron concentrations in the eastern Atlantic Ocean. Deep-Sea Res. I Oceanogr. Res. Pap. 50 (10–11), 1339–1352. http://dx.doi.org/10.1016/S0967-0637(03)00126-2.
Schlitzer, R., 2014. Ocean Data View. http://odv.awi.de.
Shiozaki, T., Ijichi, M., Kodama, T., Takeda, S., Furuya, K., 2014. Heterotrophic bacteria as major nitrogen fixers in the euphotic zone of the Indian Ocean. Glob. Biogeochem. Cycles http://dx.doi.org/10.1002/2014GB004886 (n/a–n/a).
Sparrow, M.D., Heywood, K.J., Brown, J., Stevens, D.P., 1996. Current structure of the south Indian Ocean. J. Geophys. Res. 101 (C3), 6377. http://dx.doi.org/10.1029/95JC03750.
Stramma, L., Lutjeharms, J.R.E., 1997. The flow field of the subtropical gyre of the South Indian Ocean. J. Geophys. Res. 102, 5513–5530. http://dx.doi.org/10.1029/96JC03455.
Swart, N.C., Lutjeharms, J.R.E., Ridderinkhof, H., de Ruijter, W.P.M., 2010. Observed characteristics of Mozambique Channel eddies. J. Geophys. Res. 115 (C9). http://dx.doi.org/10.1029/2009JC005875 (C09006).
Tanaka, T.Y., Chiba, M., 2006. A numerical study of the contributions of dust source regions to the global dust budget. Global Planet. Change 52 (1–4), 88–104. http://dx.doi.org/10.1016/j.gloplacha.2006.02.002.
Toole, J.M., Warren, B.A., 1993. A hydrographic section across the subtropical South Indian Ocean. Deep-Sea Res. I Oceanogr. Res. Pap. 40 (10), 1973–2019. http://dx.doi.org/10.1016/0967-0637(93)90042-2.
Vu, H.T.D., Sohrin, Y., 2013. Diverse stoichiometry of dissolved trace metals in the Indian Ocean. Sci. Rep. 3, 1745. http://dx.doi.org/10.1038/srep01745.
Ward, B.A., Dutkiewicz, S., Mark Moore, C., Follows, M.J., 2013. Iron, phosphorus, and nitrogen supply ratios define the biogeography of nitrogen fixation. Limnol. Oceanogr. 58 (6), 2059–2075. http://dx.doi.org/10.4319/lo.2013.58.6.2059.
Wedepohl, K.H., 1995. The composition of the continental crust. Geochimica et Cosmochimica Acta 59 (7), 1217–1232. http://dx.doi.org/10.1016/0016-7037(95)00038-2.
Witt, M. (2003), Studies of trace metals in the atmosphere, Unpublished Ph.D Dissertation, University of East Anglia, Norwich, UK
Witt, M., Baker, A., Jickells, T., 2006. Atmospheric trace metals over the Atlantic and South Indian Oceans: investigation of metal concentrations and lead isotope ratios in coastal and remote marine aerosols. Atmos. Environ. 40 (28), 5435–5451. http://dx.doi.org/10.1016/j.atmosenv.2006.04.041.
Witt, M.L.I., Mather, T.A., Baker, A.R., De Hoog, J.C.M., Pyle, D.M., 2010. Atmospheric trace metals over the south-west Indian Ocean: total gaseous mercury, aerosol trace metal concentrations and lead isotope ratios. Mar. Chem. 121 (1–4), 2–16. http://dx.doi.org/10.1016/j.marchem.2010.02.005.
Wong, A.P.S., 2005. Subantarctic mode water and Antarctic intermediate water in the South Indian Ocean based on profiling float data 2000–2004. J. Mar. Res. 63 (4), 789–812. http://dx.doi.org/10.1357/0022240054663196.
Zamora, L.M., Landolfi, A., Oschlies, A., Hansell, D.A., Dietze, H., Dentener, F., 2010. Atmospheric deposition of nutrients and excess N formation in the North Atlantic. Biogeosciences 7, 777–793. http://dx.doi.org/10.5194/bg-7-777-2010.